

DAMAGE EVALUATION OF GLASS FIBER REINFORCED POLYMER DECKS USING  
ACOUSTIC EMISSIONS

By

RAFAEL ASENCIO

A THESIS PRESENTED TO THE GRADUATE SCHOOL  
OF THE UNIVERSITY OF FLORIDA IN PARTIAL FULFILLMENT  
OF THE REQUIREMENTS FOR THE DEGREE OF  
MASTER OF ENGINEERING

UNIVERSITY OF FLORIDA

2011

© 2011 Rafael Asencio

To my wife, Erin, my daughter, Clare and son, Rafi

## ACKNOWLEDGMENTS

The author thanks Dr. Hamilton, my advisor and principal committee member, for his guidance and patience during this process and committee members Dr. Consolazio and Dr. Cook. The author acknowledges and thanks the Florida Department of Transportation (FDOT) for providing funding for this project. Much of the laboratory work for this project was conducted at the FDOT Marcus H. Ansley Structures Research Center and the author would like to express appreciation to David Allen, Stephen Eudy, Sam Fallaha, Tony Hobbs, Will Potter, Paul Tighe, David Wagner, and Chris Weigly for their assistance and input.

Dr. Plunkett and Kansas Structural Composites inc. is thanked for the donation of GFRP deck samples.

# TABLE OF CONTENTS

	<u>page</u>
ACKNOWLEDGMENTS.....	4
LIST OF TABLES.....	7
LIST OF FIGURES.....	8
ABSTRACT .....	11
CHAPTER	
1 INTRODUCTION .....	13
2 BACKGROUND .....	15
GFRP Deck Design and Fabrication.....	15
Pultruded deck panel (Deck A).....	15
Preform molds deck panel (Deck B).....	16
Wet lay-up deck panel (Deck C).....	16
GFRP Bridge Deck Structural Behavior.....	17
Acoustic Emission.....	17
AE fundamentals .....	18
Equipment and settings.....	19
Evaluation methods.....	19
Field testing.....	20
3 TEST SETUP AND SPECIMEN DESIGN AND CONSTRUCTION .....	24
Span and Support Configuration.....	24
Specimen Design and Construction.....	25
4 INSTRUMENTATION .....	29
Strain Gages.....	29
Load and Displacement Gages.....	30
Acoustic Emission Sensors.....	30
Disp 16 System.....	31
5 TEST PROCEDURE.....	35
Service Loading (UST and DST) .....	35
Ultimate Loading (ULT).....	36
6 ULTIMATE STRENGTH TEST-RESULTS AND DISCUSSION.....	38
Deck A Positive Bending (A_P) .....	38

Deck A Negative Bending (A_N).....	40
Deck B Positive Bending (B_P) .....	41
Deck B Negative Bending (B_N).....	42
Deck C Positive Bending (C_P).....	43
Deck C Negative Bending (C_N) .....	44
7 ANALYSIS OF AE TEST DATA USING RECOVERY RATIO ANALYSIS .....	57
8 BELLE GLADE TEST .....	65
Sensor Locations .....	65
Relative Ratio Analysis on Belle Glade Bridge Data.....	65
9 SUMMARY AND CONCLUSIONS.....	70
LIST OF REFERENCE.....	72
BIOGRAPHICAL SKETCH.....	75

## LIST OF TABLES

<u>Table</u>		<u>page</u>
3-1	GFRP sample dimensions (in.).....	28
4-1	Strain gage location dimensions – positive bending tests (in.) .....	33
4-2	Strain gage location dimensions - negative bending tests (in.).....	34
4-3	AE sensor location dimensions –positive bending tests (in.).....	34
4-4	AE sensor location dimensions –negative bending tests (in.).....	34
4-5	AE recording parameters.....	34
5-1	Testing sequence and rest time.....	37
5-2	Load profile characteristics.....	37
6-1	A_P stiffness.....	55
6-2	A_N stiffness. ....	55
6-3	B_P stiffness.....	55
6-4	B_N stiffness. ....	56
6-5	C_P stiffness. ....	56
6-6	C_N stiffness. ....	56
7-1	Average values from RRA and stiffness and strength ratio. ....	64
8-1	AE sensor identification and coordinates.....	69

## LIST OF FIGURES

<u>Figure</u>	<u>page</u>
2-1 Pultrusion process (Ultrafiberglass.com).....	20
2-2 Zellcomp deck panel.....	21
2-3 Preform sample beam used by Structural Composites of Melbourne (performs.com). ....	21
2-4 Structural Composites deck panel. ....	21
2-5 Wet lay-up glass fiber schedule (Kalny et al. (2004)).....	22
2-6 Fiber reinforced polymer honeycomb deck panel. ....	22
2-7 Acoustic emissions event. ....	22
2-8 Feature data gathered from a single AE waveform. ....	23
3-1 Positive bending test setup.....	26
3-2 Negative bending test setup. ....	27
3-3 Stud-in-grout connection detail. ....	28
4-1 Strain gage locations for positive bending test – soffit view.....	32
4-2 Strain gage locations for negative bending deck A.....	32
4-3 Strain gage locations negative bending test – wearing surface view.....	32
4-4 Strain gage locations negative bending tests – soffit view.....	32
4-5 Displacement gage locations positive bending setup A) elevation and B) plan view. ....	33
4-6 AE sensor locations for positive bending tests – soffit view.....	33
4-7 AE sensor locations for negative bending tests – soffit view. ....	33
5-1 UST and DST load profile.....	36
5-2 Ultimate loading test (ULT) profile. ....	37
6-1 Load-displacement plot – A_P tests. ....	45
6-2 A_P top plate buckling under load. ....	46

6-3	A_P web failure. ....	46
6-4	Load-strain plot - A_P ULT. ....	46
6-5	Load-deflection plot – A_N tests.....	47
6-6	A_N damaged web. ....	47
6-7	Damaged web location. ....	48
6-8	A_N ULT load-strain plot. ....	48
6-9	Load-displacement plot – B_P tests. ....	49
6-10	B_P test cracking pattern. ....	49
6-11	B_P cracks at failure load.....	50
6-12	Load-strain plot – B_P ULT. ....	50
6-13	Load-deflection plot B_N tests.....	51
6-14	Shear failure over support – B_N. ....	51
6-15	Shear failure location – B_N.....	51
6-16	Load-strain plot B_N ULT. ....	52
6-17	Load-displacement plot C_P tests. ....	52
6-18	Debonded zone C_P. ....	53
6-19	Load-strain plot C_P ULT. ....	53
6-20	Load-displacement plot C_N tests.....	54
6-21	Debonding failure C_N. ....	54
6-22	Load-strain plot C_N ULT. ....	55
7-2	Specimen B_P AE data unfiltered. ....	61
7-3	Specimen B_P AE filtered AE data.....	62
7-4	Filtered data used in AE ratio analysis calculations.....	62
7-5	Average DST and UST values for A) positive and B) negative bending tests. ...	63
7-6	RRA plot for positive bending tests – all specimens. ....	63

7-7	RRA plot for negative bending tests – all specimens.....	64
8-1	Bridge site A) aerial photo and B) detailed site plan. ....	67
8-2	AE sensor and strain gage locations on the deck panels. ....	68
8-3	AE and influence ratio calculations for LC 4 front wheel.....	68
8-4	AE data from bridge test LC4. ....	68
8-5	Sample RRA results for bridge load test.....	69

Abstract of Thesis Presented to the Graduate School  
of the University of Florida in Partial Fulfillment of the  
Requirements for the Master of Engineering

DAMAGE EVALUATION OF GLASS FIBER REINFORCED POLYMER DECKS USING  
ACOUSTIC EMISSIONS

By

Rafael Asencio

December 2011

Chair: Trey Hamilton  
Major: Civil Engineering

Glass fiber-reinforced polymer (GFRP) decks are being used as a replacement for bridge decks, due to their light weight, fast installation time, and high strength. Several different types of deck systems are available for commercial use. The nature of the resin and glass materials of the decks results in a brittle and catastrophic failure mode. Due to this failure mode and the geometry of different deck systems, traditional structural evaluation methods such as deflection and strain may not detect possible damage in the material, which could lead to a failure. In this investigation a non-destructive detection method, acoustic emissions (AE) was used to develop a possible evaluation method for in-service GFRP bridge decks. Lab test setups were designed to replicate the positive and negative bending experienced by an in-service deck system. Three different deck systems were tested in both setups. A testing load procedure was developed based on similar testing of in-service GFRP tanks. The testing consisted of service-level loading of undamaged and damaged samples. Damage was induced on the samples by loading them to capacity in the test setups. AE data were collected during all the loadings as well as strain and deflection data. The strain and deflection data were analyzed and revealed linear behavior in all the samples up to failure. The

AE data were analyzed using a structural evaluation method adapted from the Calm ratio and the load ratio, recovery ratio analysis (RRA). Calm ratio is the ratio of a selected feature AE activity during the unloading to the AE activity during the loading. The load ratio is the ratio of the load at the onset of AE activity to the previous maximum load experienced by the specimen. RRA was successful in the lab test and was then used on data collected during a bridge load test of the Hillsboro canal bridge.

## CHAPTER 1 INTRODUCTION

Florida has the largest inventory of moveable bridges in the nation, with a total of 148, of which 91% are bascule, 7% are swing and 2% are lift bridges. Most employ open grid steel decks as a riding surface for part of their span (National Bridge Inventory 2008). Compared to solid bridge decks, steel grid decks have several advantages: they can be assembled in the factory, they are light weight, and they are easy to install. Unfortunately, worn steel grid decks have high maintenance costs and provide poor skid resistance, especially when wet. As a possible option to replace the worn steel grid decks, the Florida Department of Transportation (FDOT) is investigating the possibility of using glass-fiber reinforced polymer (GFRP) decks. GFRP deck panels can be designed and manufactured to meet weight and dimensional requirements of a bridge, allowing direct replacement of steel grid decks

GFRP bridge decks are relatively new to the bridge industry. One concern regarding GFRP deck systems is their durability and field performance. Developing Non-Destructive Evaluation (NDE) methods that can be used to monitor the GFRP decks is important to ensure long-term performance is monitored and documented.

My work focuses on the use of acoustic emission (AE) to inspect GFRP decks. AE has been used extensively to assess the structural integrity of GFRP pressure tanks and vessels. Testing of these vessels has been conducted using ASTM standards. . These standards were used as a starting point in the development of AE test methods and evaluation criteria for GFRP bridge decks.

Three commercially available GFRP bridge decks were tested in flexure at service load levels and to ultimate strength. Service level loads were used with AE inspection

to determine if damage could be detected. Relative ratio analysis (RRA) was derived from a previously proven method for the evaluation of the AE data. In this thesis, the RRA method was derived and implemented first on laboratory test data and then on the AE data collected during a bridge load test of a recently installed GFRP deck.

## CHAPTER 2 BACKGROUND

Over the past 15 years, more than 100 bridges in the United States have been rehabilitated using FRP composites (Reeve 2010). The materials' light weight, corrosion resistance and fast installation time are the main advantages over conventional deck systems. In 1996, the first glass fiber reinforced polymer (GFRP) bridge was installed over a creek in Kansas (O'Connor 2008). Since then, GFRP has been used in a variety of vehicular bridge decks.

### **GFRP Deck Design and Fabrication**

GFRP deck designs and fabrication processes are manufacturer specific. Consequently, the details of components and production are usually proprietary. Samples used in this investigation were manufactured using the following assembly methods: pultrusion, wet layup, and preform molds.

#### **Pultruded deck panel (Deck A)**

In a typical pultrusion process, flexible glass fiber reinforcement is drawn in varying orientations and sequences with a manufacturer specific vinyl/ester resin through a die to construct a continuous element of constant cross section (Figure 2-1). Longitudinal reinforcement is provided by the glass fibers in the roving racks; the mats can have various fiber orientations as needed for the particular design. Zellcomp deck is the pultruded deck used in this investigation and will be referenced as deck A. Zellcomp deck is pultruded in two separate pieces and is available in 5, 7, and 9 in. depths. (Figure 2-2). The depth of the deck used in this research is 5 in. The bottom panel is composed of a bottom plate and four I-shaped sections (hereinafter referred to as "webs") that were pultruded as a single unit. The top plate was a pultruded sheet

that provides the wearing surface and transfers wheel loads to the webs. Top plates were attached to the bottom panel using self-tapping countersunk screws; the top plate is typically attached during the installation of the bridge deck.

### **Preform molds deck panel (Deck B)**

Stay-in-place preforms are used in the wet lay-up assembly process to support the wet mats during the curing process. They are made from polyurethane foam molded into the desired shape to create the cross-section. This method was developed for the boating industry (Figure 2-3). The assembly process is similar to the wet layup process but utilizes foam forms, which are made of 2 pound per cubic foot floatation-grade polyurethane foam, to hold the shape of the cross-section until the resin (preforms.com 2011). The deck is manufactured with threaded sleeves that are used to attach the deck to the bridge superstructure with clips.

Deck B was manufactured by Structural Composites, Inc. and used trapezoidal preforms to manufacture its GFRP deck (Figure 2-4). The preform was used to hold the wet lay-up fiber in place during the cure period. The depth of the deck used for this investigation was 5 in.

### **Wet lay-up deck panel (Deck C)**

Wet lay-up is a fabrication technique that arranges layers of the glass fiber mats and resin in a prescribed sequence. The type of glass reinforcement and the orientation of the fibers are selected by the manufacturer (Figure 2-5). One type of deck that is constructed using wet lay-up is the GFRP honeycomb sandwich deck. The deck consists of a honeycomb core bonded between two flat sheets of GFRP using vinyl ester resin (Figure 2-6). (Kalny et al. 2004) Deck panels are typically manufactured with pockets to accommodate stud connectors. The fiber-reinforced polymer

honeycomb panels (FRPH) used in this investigation were manufactured by Kansas Structural Composites, Inc.

### **GFRP Bridge Deck Structural Behavior**

A number of GFRP deck system's structural behaviors have been investigated. Prachasaree et al. (2009) investigated in-plane and out-of-plane shear behavior of GFRP specimens and the load transfer efficiency of the joints between the adjacent specimens. Keller and Gurtler (2005) examined the bending behavior of pultruded GFRP deck in a simply supported test set-up. Alagusundaramoorthy et al. (2006) investigated the deflection behavior of GRFP in a similar set-up. Camatta and Shing (2010) also tested FRPH deck and found the deck failure to occur in the bond between the core and the face panels. Brown and Berman (2010), Cousins et al. (2009), Vyas et al. (2009), Kalny et al. (2004), and Chen and Davalos (2010), while testing different GFRP decks, reported similar behavior when approaching the specimen's capacity; the tested deck systems failed suddenly, usually preceded by audible cracking.

Hong and Hastak (2006) indicates that the main problems found in FRP decks are debonding, delamination, and cracking of the wearing surface. No specific inspection, repair, or maintenance specifications or recommendations, however, are currently available. Telang et al. (2006) recommends the use of visual and tap-test methods as a suitable inspection method.

### **Acoustic Emission**

Acoustic emissions (AE) evaluation is a widely used non-destructive evaluation (NDE) method for detecting damage in materials such as FRP liquid storage tanks (Fowler et al. 1989). In addition, a number of researchers have begun to use AE to evaluate GFRP bridge decks (Kalny et al. (2004), Gostautas et al. (2005), and Cole et

al. (2006)). The principle behind AE is that fiber rupture and resin cracking—indicators of structural damage—emit stress waves in the structure that can be detected by sensors that are resonant in the frequency range in which these stress waves occur. Features of these stress waves can be used to distinguish them as genuine emissions from damage rather than background noise or other spurious events. The following sections provide a brief description of AE fundamentals along with details of recent AE testing that was conducted on GFRP bridge decks.

### **AE fundamentals**

Acoustic emissions waves are elastic waves produced by the release of stored strain energy caused by fracture in the material. The release of energy causes an elastic wave in the material detectable by a piezoelectric sensor, which converts the physical motion into an electrical signal. Figure 2-7 illustrates the AE detection process in which the wave is detected by the sensor and analyzed by the instrument. Features of the wave shown in Figure 2-8 are recorded by the AE system. *Threshold* is the minimum amplitude that must be reached by the event for it to be analyzed. Threshold values are typically set based on the material and the testing conditions, events that do not exceed the threshold are ignored. *Energy* (also signal strength) refers to the area under the AE wave form. *Amplitude* is the peak voltage of the event and is expressed in decibels rather than voltage (Grosse and Ohtsu 2008).

Acoustic emissions are caused by the formation of cracks in the material created during the release of strain. The Kaiser effect states that if a sample is loaded, unloaded and then reloaded under the same conditions, AE events should not be detected until the previous load peak is reached. This condition is typically satisfied in most materials if no permanent damage, the presence of significant AE at a lower load

than previously experienced by the specimen, has occurred in the specimen. Felicity effect is the breakdown of the Kaiser in which significant AE occurs at a load level below the previous maximum. The Felicity ratio (FR) is a measure of the significance of this effect and related damage to the sample; it is the ratio of load at the onset of AE activity to the previously achieved load. Therefore, an FR of 1.0 or greater is viewed as no damage; an FR less than 1.0 may be indicative of cumulative permanent damage (Gostautas et al. 2005).

### **Equipment and settings**

In previous tests of GFRP decks, Cole et al. (2006), Gostautas et al. (2005), and Kalny et al. (2004) used 150 kHz sensors and broad-band sensors with a response range of 100 to 2100 kHz; both were pre-amplified for a 40 dB gain. AE monitoring was conducted in this research using a Physical Acoustic Corp. (PAC) system. The threshold was set to 45 dB. PAC data acquisition (DAQ) system with MISTRAS AE-DAQ software was used to collect and record the data. Each sensor was coupled to the surface using hot melt glue, which is a typical attachment method for AE sensors.

### **Evaluation methods**

Calm ratio, comparison analysis, and intensity analysis have been used to evaluate the AE data from different tests. The calm ratio, the ratio of a selected feature AE activity during the unloading to the AE activity during the loading, is evaluated by plotting it against the load ratio, the ratio of load at the onset of AE activity to the maximum load experienced by the structure. Kalny et al. (2004) used AE to monitor the FRPH sample during testing. Comparison analysis compares the data to a previous loading and is based on Felicity ratio and Kaiser Effect. Intensity analysis has been

used in the pressure vessel industry and has been investigated in some deck monitoring. (Gostautas et al. 2005).

### Field testing

AE testing on GFRP bridge components has been limited primarily to laboratory tests. A small number of AE tests have been conducted in the field on both GFRP and concrete structures. In a field test of a GFRP deck by Joeng et al. (2006), the deck was tested using a load truck. Turner et al. (2004) performed a load test on a GFRP deck using load trucks near HS 25 load level. Luo et al. (2004) used AE to evaluate the structural integrity of an in-service concrete bridge pier on a train bridge. Calm ratio was used in the analysis of the structure and a new index was developed to replace the load ratio, ratio of Repeated Train load at the onset of AE activity to Relative maximum load for Inspection period (RTRI). The introduction of this factor makes it possible to use the calm ratio analysis when the historic maximum load on the structure was not known.

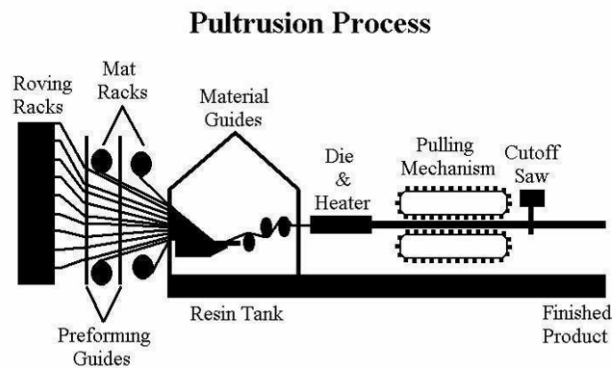


Figure 2-1. Pultrusion process (Ultrafiberglass.com).

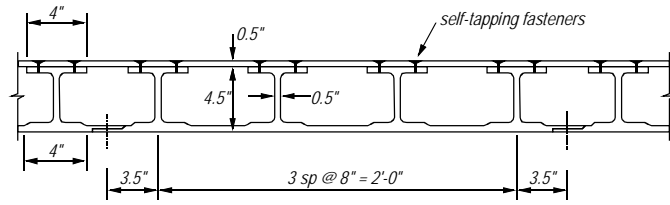


Figure 2-2. Zellcomp deck panel.



Figure 2-3. Preform sample beam used by Structural Composites of Melbourne (performs.com).

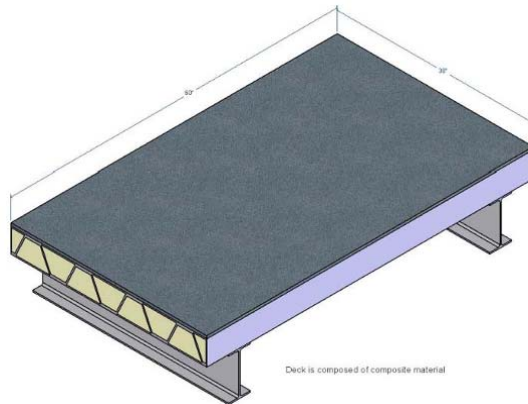


Figure 2-4. Structural Composites deck panel.

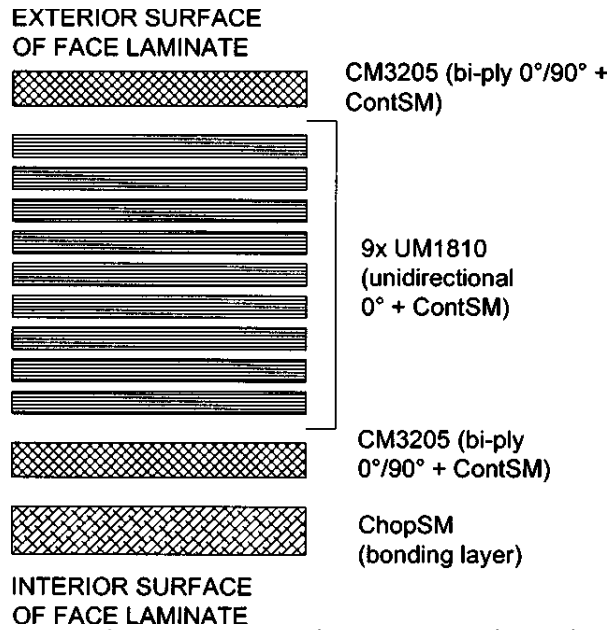


Figure 2-5. Wet lay-up glass fiber schedule (Kalny et al. (2004).

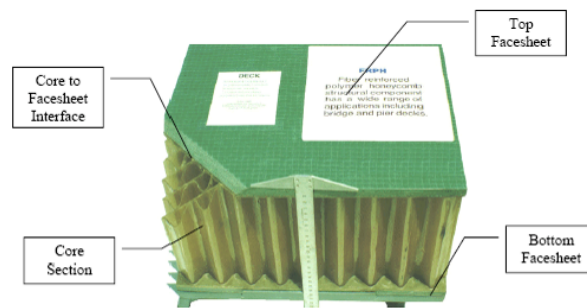


Figure 2-6. Fiber reinforced polymer honeycomb deck panel.

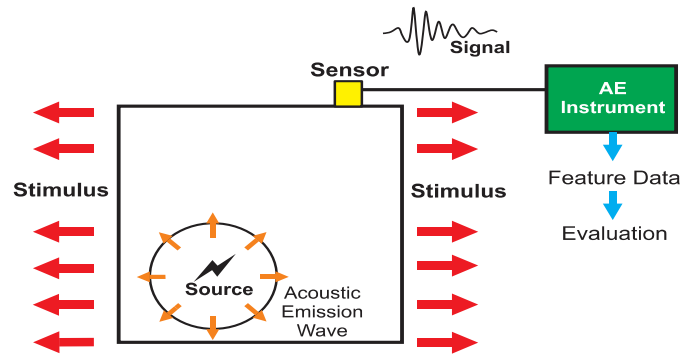


Figure 2-7. Acoustic emissions event.

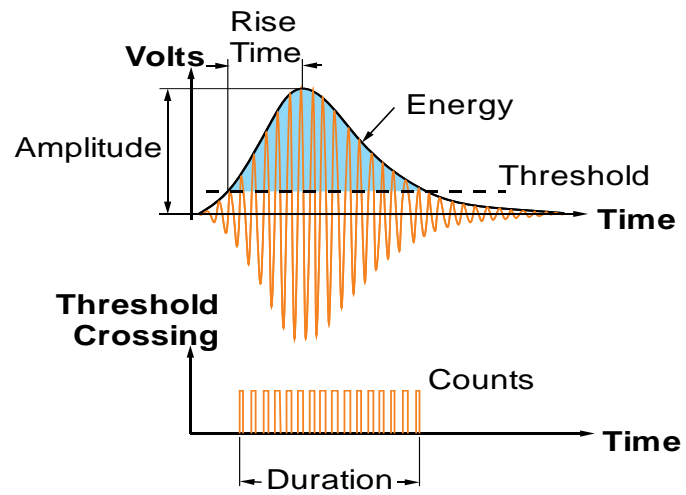


Figure 2-8. Feature data gathered from a single AE waveform.

## CHAPTER 3 TEST SETUP AND SPECIMEN DESIGN AND CONSTRUCTION

The primary focus of this research was to develop an AE evaluation that can be applied to in-service GFRP decks. Because GFRP deck panels are typically designed to span continuously over several supports, capturing both the positive and negative bending behavior of each deck type during structural testing was necessary to ensure that the damaged deck condition was as close to actual field conditions as possible. In addition, concentrated loading was used to simulate wheel loading that typically controls the design of a bridge deck.

### **Span and Support Configuration**

The test setup was designed to simulate the actions caused by wheel loads on a GFRP deck such as the Hillsboro canal crossing bridge in Belle Glade, FL (Singh et al. 2010). In lieu of testing a single continuous panel, separate tests to independently evaluate the positive and negative bending behavior and associated AE activity were conducted. Figure 3-1 shows the positive bending setup. In this configuration the panels were tested in the upright position to simulate positive bending in the typical installation. Wheel loads were approximated by applying the load through a 10-in. by 20-in. bearing pad.

Figure 3-2 shows the negative bending test setup. The panels were inverted in the test setup to simulate negative bending. Before testing, the deck-to-girder connection as was typical for that system. Wheel loads in this setup were simulated by placing two 10 in. by 10 in. bearing pads between the deck and supports. The load was applied through the spreader beam which was similar in width to the bridge girders and were stiffened by welding plates connecting the webs and flanges in four locations

along the beam. Neoprene bearing pads were used at support and load application point to reduce ambient and mechanical noise from contact with the supports and the hydraulic actuator; this reduced spurious AE activity.

### **Specimen Design and Construction**

Three different types of commercially available GFRP deck, designed and fabricated by Zellcomp, Structural Composites of Melbourne, and Kansas Structural Composites Inc. were selected for testing. Each deck was tested independently in positive and negative bending test setups to capture the individual behavior of each action. The specimen depth was 5 inches and the dimensions for each deck type were the same for positive and negative bending specimens and are listed in Table 3-1.

The positive bending specimen was A\_P. To simulate negative bending (flexural tension in the top plate), the loading frame was fitted with a shear stud. This stud was grouted into specimen A\_N as shown in Figure 3-3

The positive bending sample (B\_P) had a wearing surface applied by the manufacturer. The negative bending sample (B\_N) had a significant amount of cracking on the wearing surface; this was present prior to testing. The debonding of the wearing surface during the negative bending testing of the sample resulted in inaccurate strain data from the sensors on the wearing surface. For B\_N the attachment mechanism to the girder was a series of bolts and clips that secured the girder to the deck. These were placed at the wrong location, away from the girder connection, however and were not used in the testing.

Positive bending specimen (C\_P) was a solid section of FRPH. The negative bending specimen (C\_N) used a single attachment point composed of a recessed steel flange into the deck which fastens the deck to the girder using a welded stud to the

girder. Additional information on the connections can be found in Asencio and Hamilton (2011).

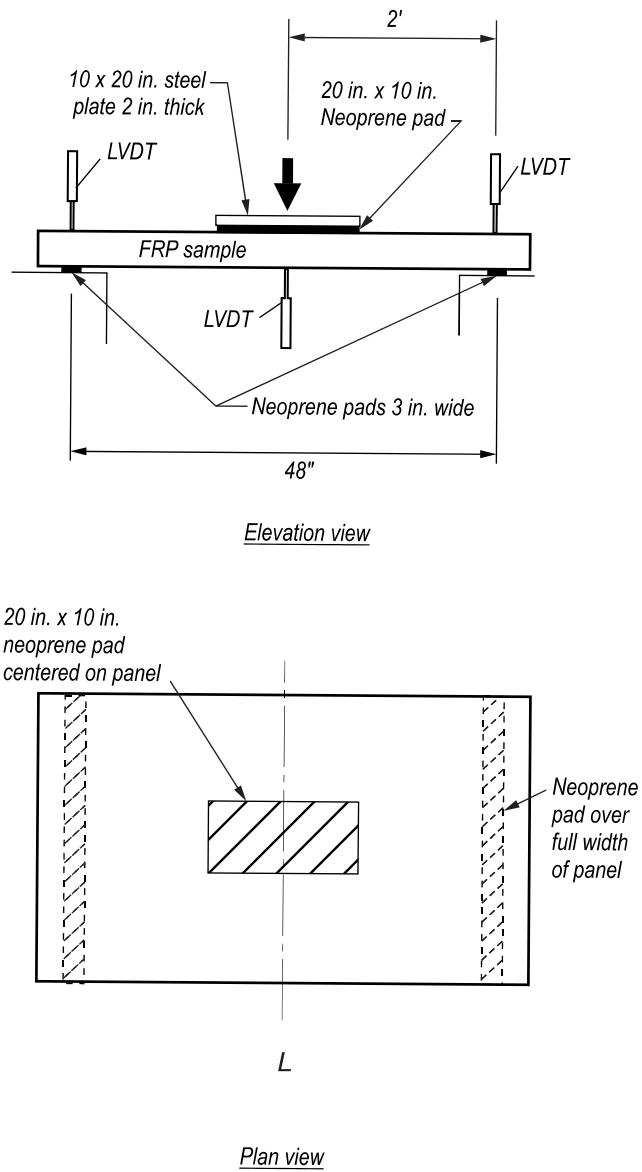
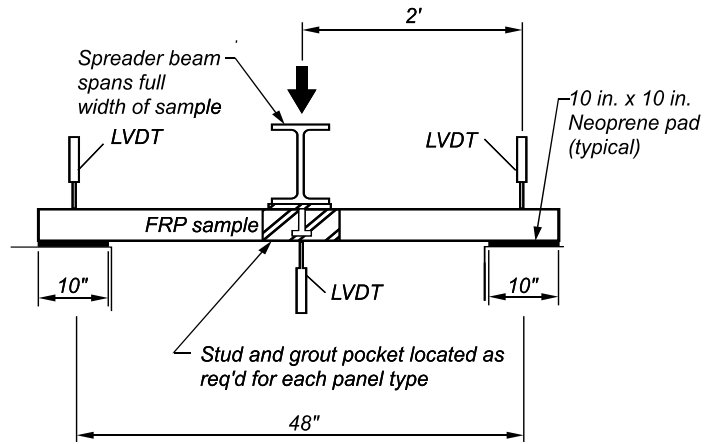
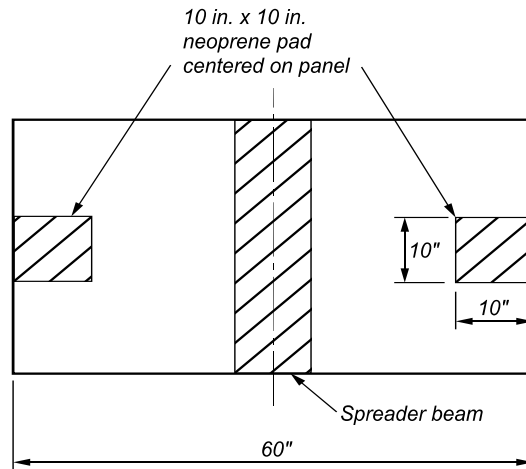


Figure 3-1. Positive bending test setup.



*Elevation view*



*Plan view*

Figure 3-2. Negative bending test setup.

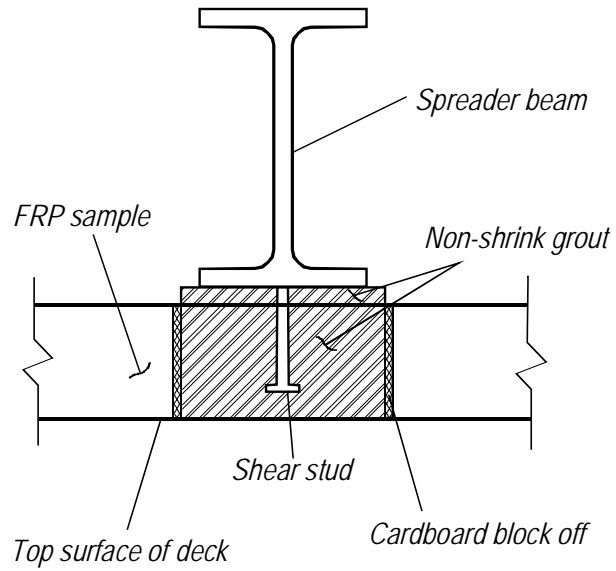


Figure 3-3. Stud-in-grout connection detail.

Table 3-1. GFRP sample dimensions (in.).

Specimen	Length	Width
A	55	33
B	55	36
C	60	36

## CHAPTER 4 INSTRUMENTATION

GFRP deck specimens were instrumented with strain gages, displacement gages, and load cells to measure the deck response to service and ultimate loads. Acoustic emission (AE) testing must be conducted during loading. Consequently, AE specimens had sensors in place during the loading and unloading process.

### **Strain Gages**

Strain was measured using quarter-bridge, 120-ohm resistance, 6 mm long gages. This gage size had been used successfully on recent tests of similar GFRP deck systems and on recent bridge load tests on a GFRP bridge deck. Using the same gages in the lab tests helped maintain consistency between the bridge and the lab tests results.

Strain measurement focused on measuring flexural tensile strains on the extreme fiber of the section. Because the decks were tested in either positive or negative bending, tensile strains occurred on opposite faces of the deck depending on the setup used. Positive bending test setup and strain gage locations are presented in Figure 4-1 and Table 4-1. Gages were arranged to capture the variation in strain over the width of the section that was expected to occur due the concentrated nature of the load.

In the negative bending test set-up, the strain gages were placed on the wearing surface of the specimens. Deck A has been shown to have very little composite action between the top plate and bottom panel (Cousins et al. 2009), therefore the strain gages S1-S3 for Deck A were placed on the flanges of the bottom panel as shown in Figure 4-2 in order to measure tensile strains under negative bending.

The top surface strain gage locations for Decks B and C are shown in Figure 4-3. Strain gage locations were selected for each of these systems to accommodate the varying web configurations. Gages S1, S2, and S3 were placed on the top surface of the sample. The other five gages were placed on the soffit of the deck (Figure 4-4 and Table 4-2).

### **Load and Displacement Gages**

Displacement gages were arranged for the positive bending setup as shown in Figure 4-5. For Decks B and C, the gages were placed along the center line of the samples; the gages were offset from the center line for Deck A because the top plates had been observed to separate slightly from the bottom panel under high loads. The offset displacement gage location allows for the measurements to be based only on the bottom panel deflections. The load in the configuration is measured with an inline load cell placed between the load actuator and the specimen.

### **Acoustic Emission Sensors**

Acoustic emission sensors were placed only in locations that would typically be accessible in a field application. Sensors were placed on the soffit of the samples under and away from the load and under the different features of each sample (Figure 4-6 and Table 4-3).

Damage was expected to occur in the area surrounding the loading girder in the negative bending test setup. Consequently, AE sensor locations for the negative bending tests were similar to those of the positive bending test, but adjusted to accommodate the placement of the girder. As in the positive test setup, the sensor locations were chosen to capture the AE activity between the load point and the supports while being attentive to different features in each deck design. Figure 4-7

shows the negative bending setup and the specific locations related to the different decks are listed in Table 4-4.

Using hot glue as the couplant, the sensors were attached in accordance with ASTM E 650-97. Prior to loading, as per ASTM E 976-99, the sensor placement and data acquisition were evaluated using the pencil lead break method.

### **Disp 16 System**

The AE data acquisition system used was the DISP-16BT, manufactured by Physical Acoustics Corporation. This system used the software AEWIn E3.11 to acquire, record, and replay eight channels of feature data. The system used integral preamp piezoelectric sensors model number R15I-AST. The sensors had the capability to drive long cables without the need of a separate preamplifier. The sensors were designed for circumstances where background noise can be high with a built in filter and a 40dB preamplifier in the sensor (Physical Acoustic Corporation 2008).

Table 4-5 lists the adjustable parameters values used in this investigation. Peak Definition Time (PDT) ensures the correct identification of the signal peak for risetime and peak amplitude measurement; Hit Definition Time (HDT) ensures that each AE signal corresponds to only one hit, and Hit Lockout Time (HLT) avoids recording spurious measurements during the signal decay. (Physical Acoustics Corporation 2004) The threshold was selected after several lab tests measuring ambient noise. The sample rate was set to the maximum allowed by the machine. PDT, HDT, HLT, and Max duration settings recommended by the equipment supplier for GFRP materials were used.

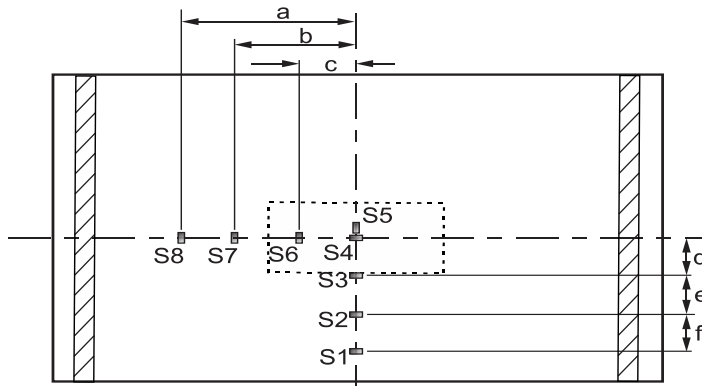


Figure 4-1. Strain gage locations for positive bending test – soffit view.

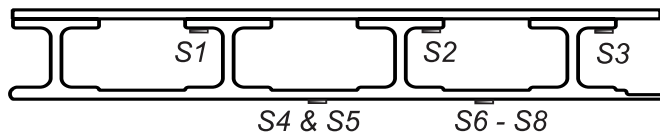


Figure 4-2. Strain gage locations for negative bending deck A.

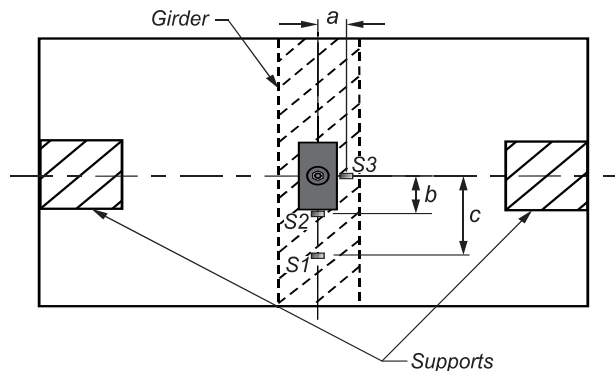


Figure 4-3. Strain gage locations negative bending test – wearing surface view.

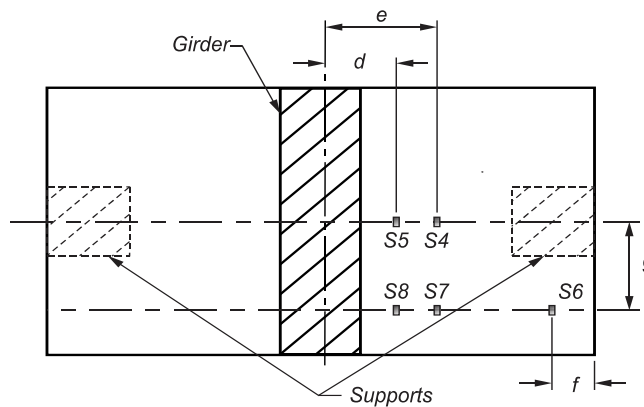


Figure 4-4. Strain gage locations negative bending tests – soffit view.

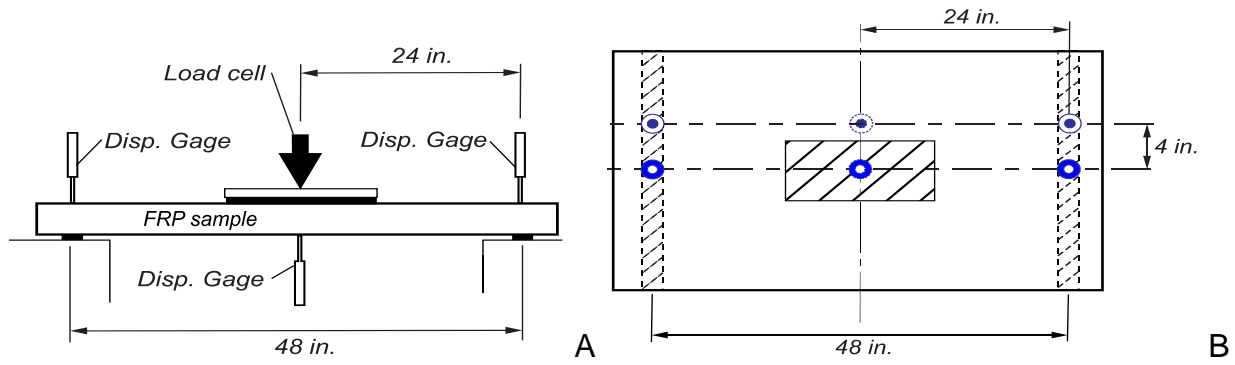
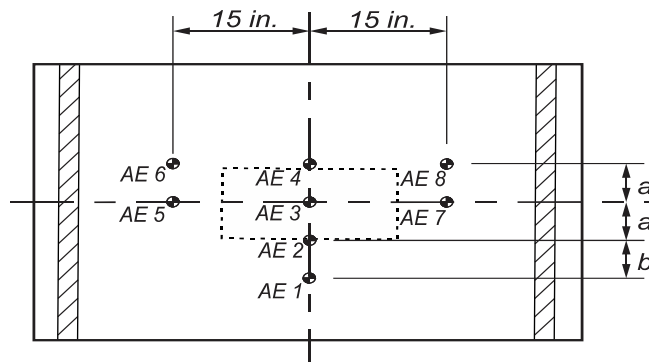


Figure 4-5. Displacement gage locations positive bending setup A) elevation and B) plan view.



Bottom View

Figure 4-6. AE sensor locations for positive bending tests – soffit view.

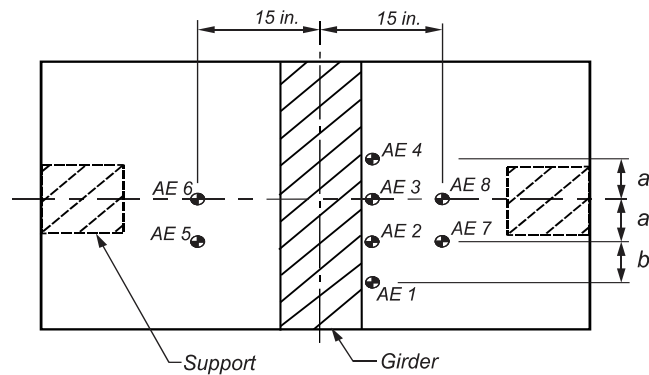


Figure 4-7. AE sensor locations for negative bending tests – soffit view.

Table 4-1. Strain gage location dimensions – positive bending tests (in.)

Specimen	a	b	c	d	e	f
A	12	8	4	4	4	4
B	13	9.5	5	5	4.5	4.5
C	13	9	5	5	6.5	7

Table 4-2. Strain gage location dimensions - negative bending tests (in.).

Deck Type	a	b	c	d	e	f	g
A	N/A	N/A	N/A	3.2	9.5	3.5	12
B	0.0	4.5	9.0	7.0	10.25	3.5	11
C	4.0	9.0	13	3.5	7.0	6.0	3.5

Table 4-3. AE sensor location dimensions –positive bending tests (in.).

Deck	a	b
A	4	4
B	5	6
C	5	6.5

Table 4-4. AE sensor location dimensions –negative bending tests (in.).

Deck	a	b
A	4	4
B	5	9
C	5	6.5

Table 4-5. AE recording parameters.

Threshold	45 dB
Analog filter	10 kHz-2MHz
Sample rate	10MSPS
Peak Definition Time (PDT)	35 $\mu$ s
Hit Definition Time (HDT)	150 $\mu$ s
Hit Lockout Time (HLT)	300 $\mu$ s
Max duration	1000 ms

## CHAPTER 5 TEST PROCEDURE

Multiple load tests were conducted on each specimen using three different loading profiles. The sequence of the loading profiles is shown in Table 5-1. First, the specimen was subjected to two undamaged service tests (UST) composed of three load holds. The specimen was then subjected to an ultimate load test (ULT), in which the specimen was loaded to its ultimate capacity. This was done to cause damage without completely destroying the specimen. Finally, stepwise service loads (DST) were again imposed on the damaged deck to determine how well AE could detect the damage that had occurred during the ultimate strength test. Both positive and negative bending specimens were tested using the same procedures. Load steps were separated by a brief load reduction to allow observation of Kaiser and Felicity effects during reloading. Details of the loading profile are provided in the next section.

The loading rest time requirements for each loading were designed to duplicate the field conditions experienced by a deck. The initial UST was followed by a rest period of 24 hours. A second UST was performed in order to collect data from a known undamaged previously loaded deck, which should have considerably less AE events than the initial loading.

### **Service Loading (UST and DST)**

The setup designed for the laboratory tests for both positive and negative bending test allow the sections to have different loads per deck system. Details of the development of these load steps can be found in Asencio and Hamilton (2011). The purpose of intermediate load holds was to check for Kaiser and Felicity effects, as prescribed in ASTM 1067. Figure 5-1 shows the service loading profile used for both

UST and DST. Load hold magnitudes and duration are listed in Table 5-2. To detect either Kaiser or Felicity effects and to develop undamaged AE data of the samples, two UST were performed on each sample before the ultimate loading. Samples were then loaded to ultimate capacity imposing significant damage. Following the ultimate loading test, the damaged samples were then retested (DST) using same load profile as was used for UST.

### Ultimate Loading (ULT)

The ultimate load test (ULT) was designed to provide AE data for each type of deck tested up to failure and to take the specimen to ultimate capacity to ensure significant damage had been imposed on the specimen before the follow-up DST. Figure 5-2 shows the load profile used in the ULT. The duration of each load hold was a minimum of 2 min. and was adjusted based on the live AE data observed during the loading (ASTM 1067-96). Load hold levels started at 45 kip and increased by 15 kip until capacity was reached.

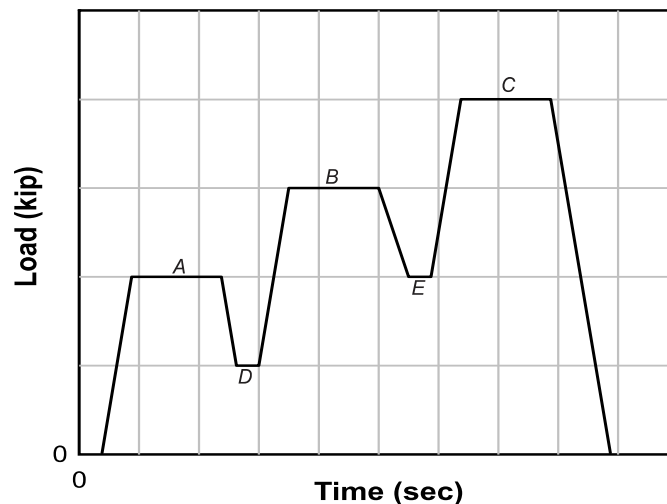


Figure 5-1. UST and DST load profile.

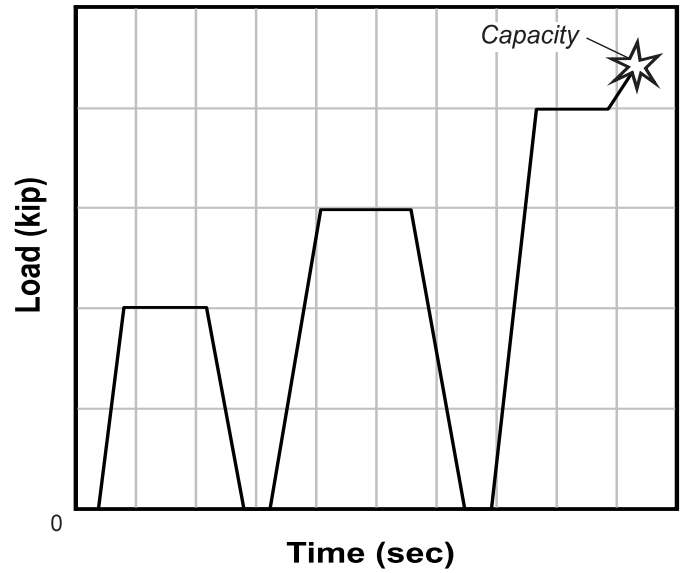


Figure 5-2. Ultimate loading test (ULT) profile.

Table 5-1. Testing sequence and rest time.

Loading Sequence	Post-Test Rest time
Initial UST	24 hr (min)
UST	30 min.
ULT	30 min.
DST	30 min.

Table 5-2. Load profile characteristics.

Load Hold	Load (kip)		Minimum Duration (sec.)
	A	B&C	
A	5	10	120
B	9	15	120
C	12	20	120
D	2.5	5	30
E	5	10	30

## CHAPTER 6 ULTIMATE STRENGTH TEST-RESULTS AND DISCUSSION

Positive and negative bending tests were conducted on each deck type. The focus of the tests was to load the specimens beyond their ultimate capacity and cause damage that might be associated with an overload in the field. This was done primarily to evaluate the effectiveness of AE in detecting the damage caused by overload. Recall that service loadings were applied both before and after each ultimate load test to assist in evaluating damage detection procedures.

In general, failure modes differed between positive and negative bending tests. The following sections describe the behavior and observations of the positive and negative bending tests conducted on the respective deck type.

Initially, the specimens were loaded using the service load profile to establish the behavior of the undamaged specimens; these will be referred to as undamaged service-load tests (UST). The ultimate loading test (ULT) was then used to impose damage and determine the ultimate load capacity. The damaged samples were then reloaded using service level loads, these tests will be referred to as damaged service load test (DST). The following sections describe the behavior during each of the three load tests including the failure mode noted during ULT. Strain data are also presented and evaluated.

### **Deck A Positive Bending (A\_P)**

Figure 6-1 shows the load-displacement response of specimen A\_P tests and include UST, SLT and DST plots. Two UST's were initially performed on the sample. During the first test, sharp audible cracking was noted as the load increased. During the service load hold, however, the deck remained quiet. Audible cracking was less

notable during the second UST and was quiet during the load hold. The second load cycle is shown in the plot and is linear, indicating that the deck remained linear-elastic during this test.

ULT load-deflection was linear up to a peak load of 72 kip. Audible cracking was noted as load was increased. In addition, when service load levels were exceeded, the top plate of the deck system was observed to deform out-of-plane between fasteners (Figure 6-2), this was an indication that the deck system was not acting compositely. Ultimate capacity was signified by both a sharp audible crack and partial loss of load, but not complete collapse. A residual capacity of 43 kip remained after the specimen load reached its ultimate limit state. The unloading portion of the ultimate loading plot is not shown below the 43 kip mark to more clearly show the service load level loadings. Visual inspection indicated that the loss of load was caused by the crushing and buckling of the webs adjacent to the loading pad (Figure 6-3).

DST shown in Figure 6-1 indicated that the web damage reduced the overall deck stiffness. Table 6-1 shows the stiffness of the specimen for each test regime as determined by linear regression of the last curve of each test. As indicated in Table 6-1, the measured stiffness was reduced by 27% from the undamaged state.

Figure 6-4 shows the ULT strain values for A\_P. The relative magnitude of the strain values at any given load indicates transverse distribution of the concentrated load. The strain under the load point (S3) was approximately twice that of the strains under the outside web (S1) which indicates that the interior webs are carrying about twice the load of the outside web. This significant difference in load is indicative of the relative flexibility of the panels connecting the webs and the marginal amount of load

distributed to adjacent webs. Linearity of the strains in S1 and S2 indicates that the system remained linear elastic up to ultimate capacity. Abrupt loss in load with little indication of softening demonstrates the brittle nature of the material.

### **Deck A Negative Bending (A\_N)**

Figure 6-5 shows the load-deflection curves for the UST, ULT, and DST load test. It was anticipated that the grout pocket may have exhibited additional audible cracking during UST. No increase in audible cracking, however, was noted over that of the positive bending test.

ULT load-deflection was initially linear with audible cracking noted at about 50 kip, which was thought to be the grout cracking. The grout was thought to provide some support due to the large deformations noted in other tests. At approximately 65 kip ULT load-deflection curve changes slope, which suggests the sample sustained a large amount of damage at that time, but the specimen supported additional load up to 76 kip when the sudden failure occurred. The residual load after reaching ultimate strength was 63 kip.

Post ULT inspection indicated that a single web directly above the supports was found to be damaged (Figure 6-6). Figure 6-7 shows the location of the damaged web in relation to the test setup. This localized failure is similar in nature and location to the failure encountered in the positive bending ULT. In this test, however, the failure resulted in little loss of global stiffness due to its localized nature. Consequently, the specimen retained its original stiffness at the lower service load levels, as indicated by the slope of the DST load-displacement curve.

Table 6-2 shows the calculated deck stiffness for each test. As previously mentioned only two of the webs were directly in contact with the supports (Figure 6-7)

one of which was crushed during ULT. The strain differential of the two webs directly under the load could not be confirmed with the strain data since one of the strain gages was damaged during assembly. In contrast the positive bending specimen lost 24% of its original stiffness after ULT and had damage to both webs under the applied load.

Figure 6-8 shows the load-strain data. The specimen initially had three strain gages, but S3, which was mounted under the web that failed, was damaged when the top plate was being replaced. S1 strain values were 35% of the S2 strains confirming transverse flexibility. The strain curves remained linear up to capacity.

### **Deck B Positive Bending (B\_P)**

Figure 6-9 shows the load displacement response of test B\_P and includes UST, SLT, and DST plots. Specimen B\_P was qualitatively noted to have significantly less audible cracking than A\_P, which was thought to be due to damping effects of the foam core.

ULT of the sample reached ultimate capacity of 112 kip, which was accompanied by a sharp audible cracking. A residual load of 92 kip was observed prior to the unloading of the sample.

During the ultimate strength test, cracks formed around the load point in the top panel (highlighted in Figure 6-10). As load was increased, the cracks grew parallel to the span and eventually merged over the supports when the ultimate capacity was reached Figure 6-11. Post ULT inspection of the specimen indicated that the bottom soffit of the sample was intact and that the top surface retained a bowl-shaped permanent deformation, indicating that the interior webs were also permanently deformed.

The difference in slope between the UST and the DST curves demonstrates the loss of stiffness after the ULT. The stiffness and stiffness ratios were calculated using linear regression for the three loadings and are presented in Table 6-3. The stiffness of the section was decreased by 30% after ULT procedure.

Figure 6-12 shows the strain values for the ULT of the B\_P. Strain gages plots were grouped by their respective positions in relation to the load pad. S1 and S2, the gages positioned away from the load, reported values 50% that of the gages directly under the pad, S3 and S4. The transverse stiffness of the deck is small and similar to Deck A.

### **Deck B Negative Bending (B\_N)**

Figure 6-13 shows B\_N results of UST, ULT and DST load-deflection plots. Specimen B\_N setup had no mechanical connection to the girder, the deck was insulated by a ½ in. neoprene pad, this contributed to the lack of audible cracking emitted by the specimen. A large crack formed over one of the supports at approximately 112 kip as indicated by the discontinuity in the ULT plot. However the specimen did not lose load and the loading continued to an ultimate capacity of 134 kip. The specimen failed abruptly and violently with a residual load of 69 kip.

Figure 6-14 shows punching shear failure over the support. The crack followed the edge of the interior web extended past the support into the deck. Figure 6-15 highlights the approximate location of the failure plane. The deck wearing surface delaminated from the deck surface and pieces can be seen on the steel support beam in Figure 6-14.

Table 6-4 shows the stiffness and the stiffness ratio for the negative bending test. The difference in stiffness between the UST and the ULT was 14% this was the only

deck system to lose significant stiffness between UST. The DST stiffness was 76% less than the UST and 62% less than the ULT. The punching shear failure caused a large loss of stiffness relative to the other deck tests.

Strain gages were placed on the road surface of the sample to capture the largest magnitude of strain during loading. During ULT, however, the road wearing surface applied by the manufacturer debonded from the deck damaging two of the strain gages. The ULT load-strain plot for the remaining undamaged strain gages is presented in Figure 6-16. The strain magnitudes were significantly less than the positive bending test strain values of the same deck type, which were nearly 10000 ( $\mu\epsilon$ ) at 112 kip. The reported strain of the negative bending test was expected to be similar in magnitude to the positive bending strains. Recorded strain values, however, were only 1200 ( $\mu\epsilon$ ) at 135 kip. This suggests that the debonded wearing surface affected the remaining strain gage and the data are not accurate.

### **Deck C Positive Bending (C\_P)**

UST, ULT and the DST results for C\_P are presented Figure 6-17. Initially two UST's were performed on specimen C\_P followed by the ULT. During the service loadings audible emissions were notably less than those from the other two deck types. During the ULT sharp audible cracking began at 70 kip load level and continued up to the ultimate capacity of 100 kip. Residual load of 80 kip was supported by the sample; the unloading portion of the curve was not shown to avoid obscuring the UST and DST results. The deck system is designed so that the compression flange delaminates from the honeycomb core, which was the observed failure mode. Delamination, however,

was not visible so coin tap testing was used to estimate extent of the delamination (outlined in blue in Figure 6-18).

The stiffness of each loading was determined by linear regression (Table 6-5). The sample's stiffness was the greatest of the three tested. The sample's stiffness was reduced by 30% after the ULT.

Figure 6-19 shows the ULT strain values. The transverse stiffness of the sample was very large in comparison to the other samples. The strain value near the outside edge of the deck (S1) had the smallest strain magnitude and it was 75% of the peak value under the concentrated load (S4).

### **Deck C Negative Bending (C\_N)**

The load-deflection plots UST, ULT, and DST are presented in Figure 6-20. During the initial UST no audible cracking was noticed. The ULT was also quiet up to the 65 kip level when audible cracking was noted, increasing up to the sudden and violent failure at 79 kip load level. Immediately after the ultimate load level was reached the system lost almost all of its strength the damage was extensive and the system only had 14 kip of residual load immediately after the failure.

The sample failed by delamination of the top from the center honeycomb section out to the support seen in Figure 6-21. The sample was designed to fail by delamination of the compression zone of the deck; however in this case the large load and the short span caused the compression zone to reach the support and the entire sheet delaminated. The failure seen in the sample would not be seen on the field because the deck would be a continuous slab and the load would never be placed that close to an unsupported edge; however the deck behavior of a delaminated sample was still of interest to the project.

The stiffness and the stiffness ratio to the UST stiffness of each of the loadings above were calculated by linear regression and listed in Table 6-6. This deck was very stiff in comparison to the other decks tested, but due to the failure mode the damaged loading had the largest decrease in stiffness of 86% after the ULT.

The strain gage data of the deck along the top of the girder are presented in Figure 6-22. In this configuration the decks transverse stiffness was not as large as in the positive bending setup. S1 only had 20% of the peak strain recorded during the ULT near the center of the specimen (S2).

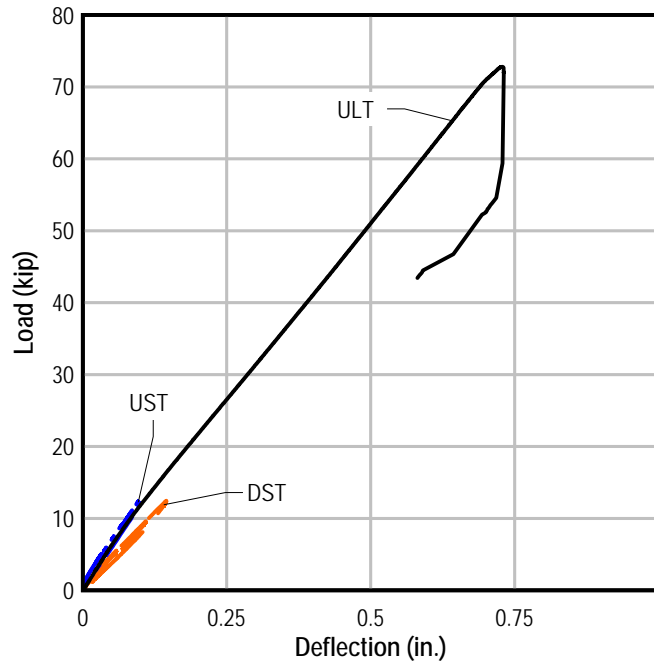


Figure 6-1. Load-displacement plot – A\_P tests.

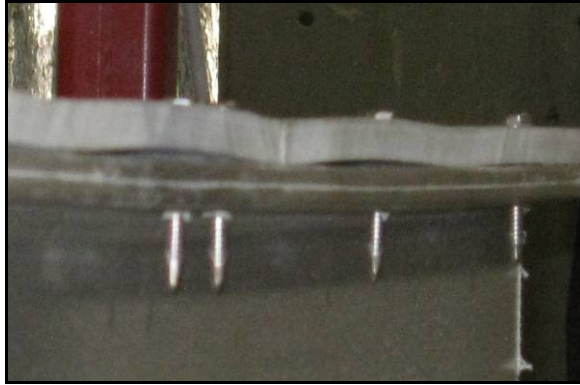


Figure 6-2. A\_P top plate buckling under load.



Figure 6-3. A\_P web failure.

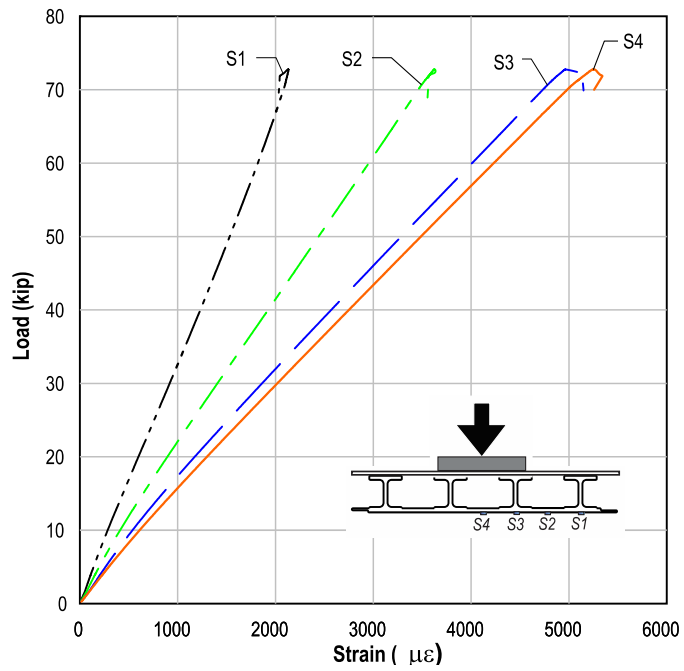


Figure 6-4. Load-strain plot - A\_P ULT.

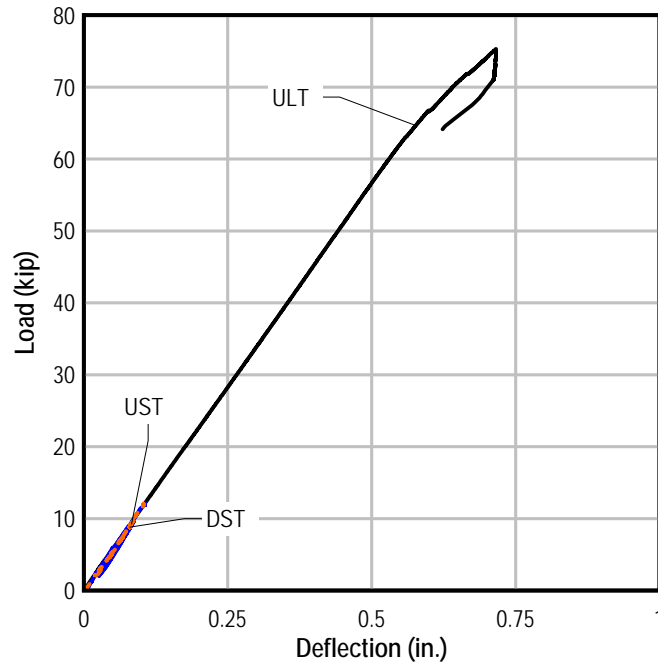


Figure 6-5. Load-deflection plot – A\_N tests.

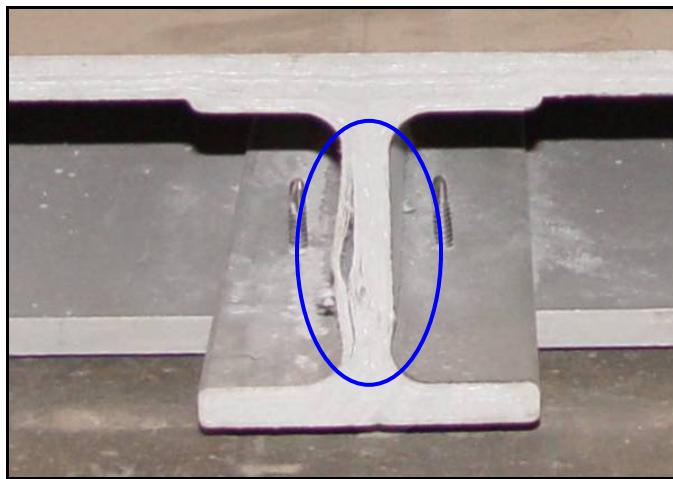


Figure 6-6. A\_N damaged web.

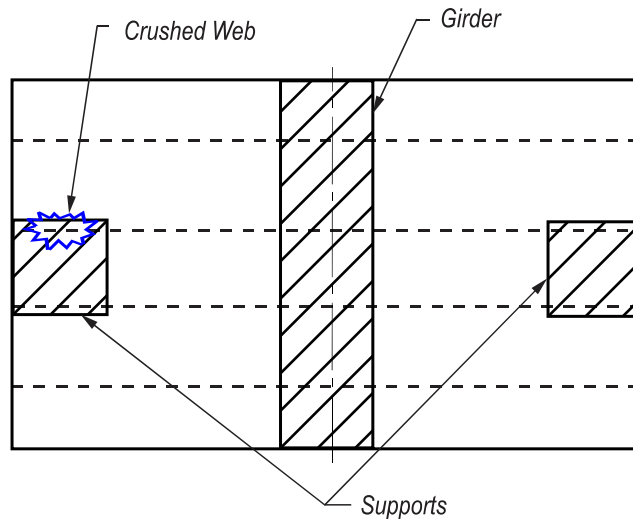


Figure 6-7. Damaged web location.

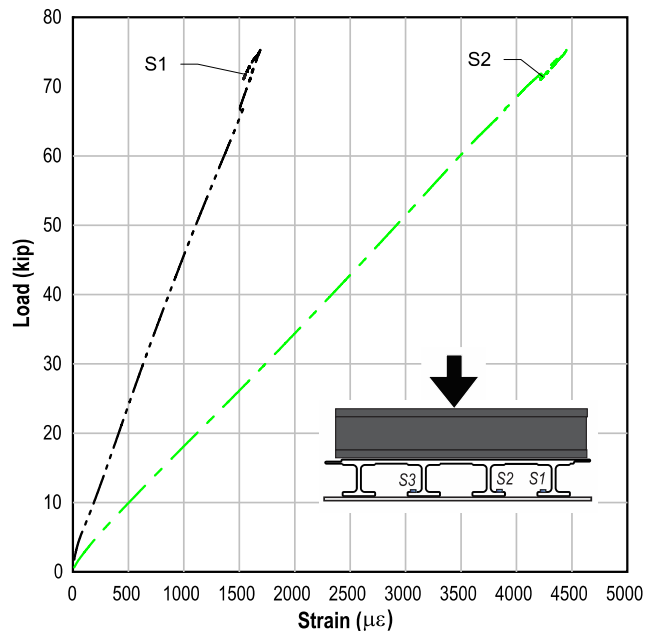


Figure 6-8. A\_N ULT load-strain plot.

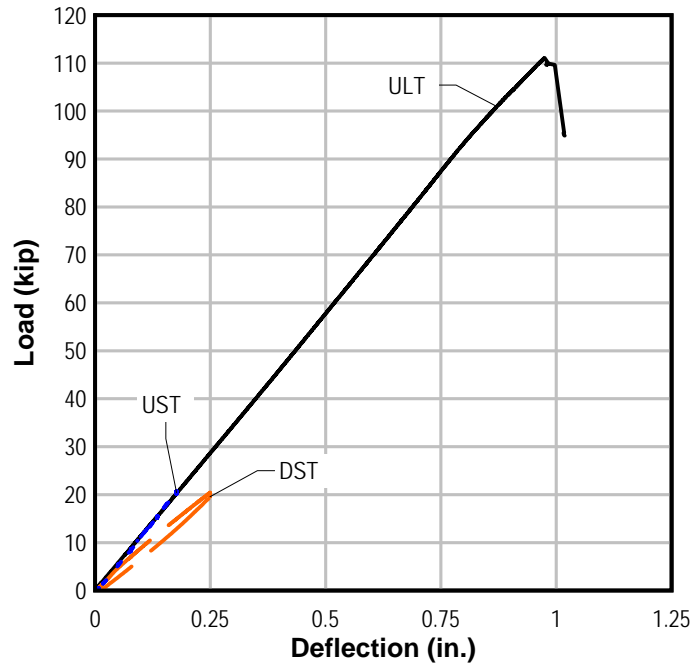


Figure 6-9. Load-displacement plot – B\_P tests.



Figure 6-10. B\_P test cracking pattern.



Figure 6-11. B\_P cracks at failure load.

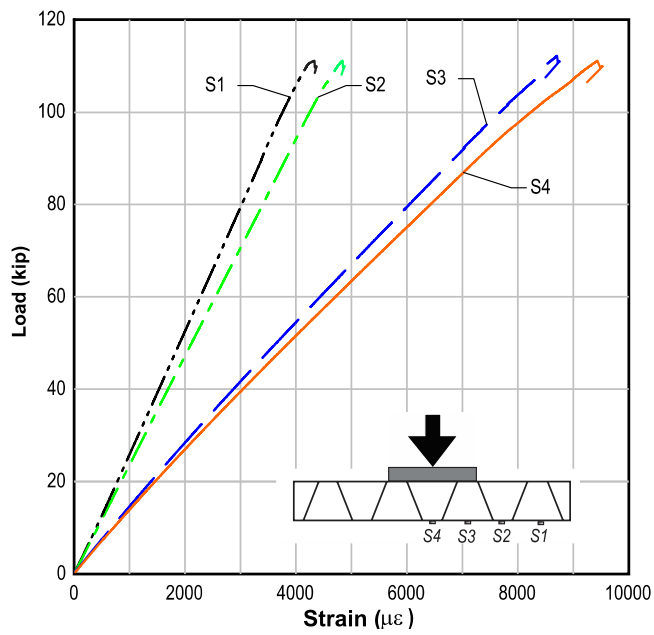


Figure 6-12. Load-strain plot – B\_P ULT.

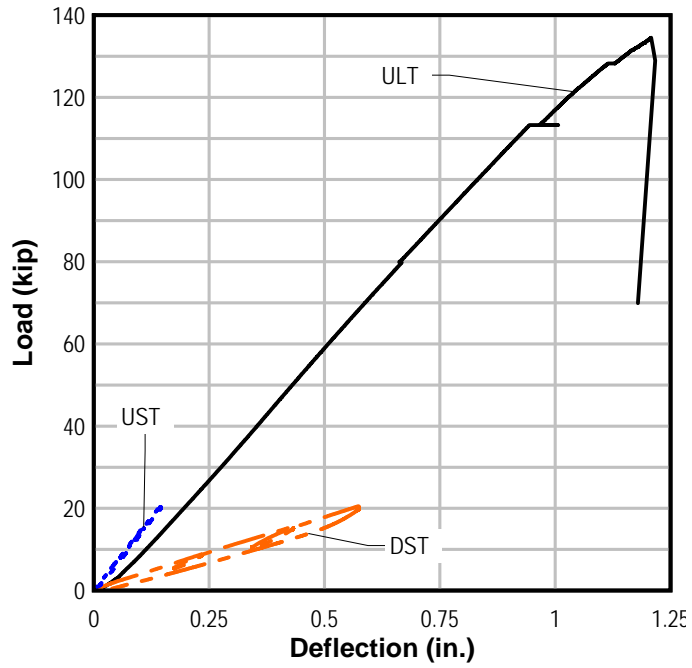


Figure 6-13. Load-deflection plot B\_N tests.



Figure 6-14. Shear failure over support – B\_N.

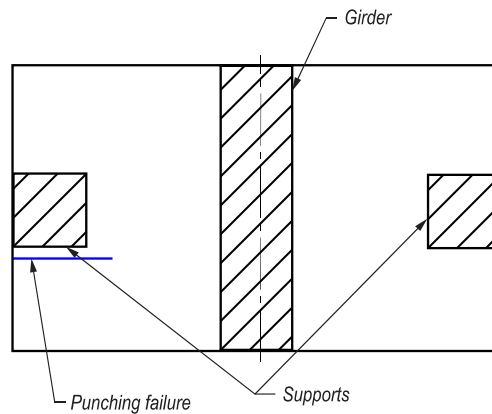


Figure 6-15. Shear failure location – B\_N.

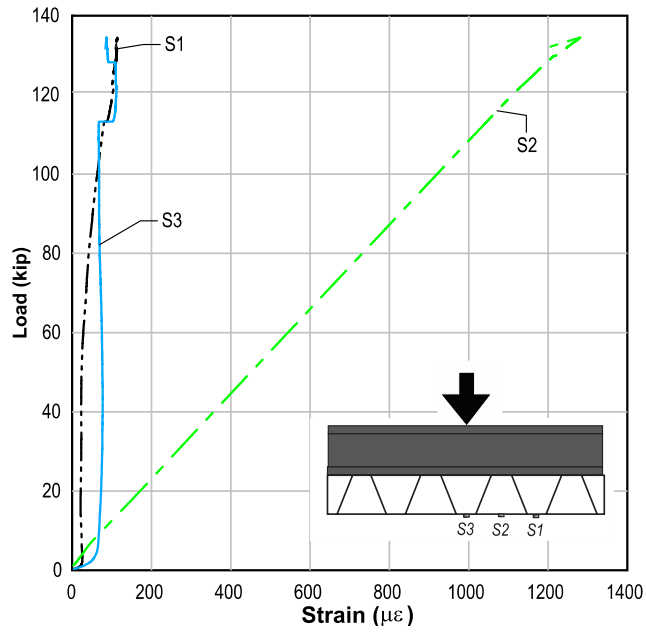


Figure 6-16. Load-strain plot B\_N ULT.

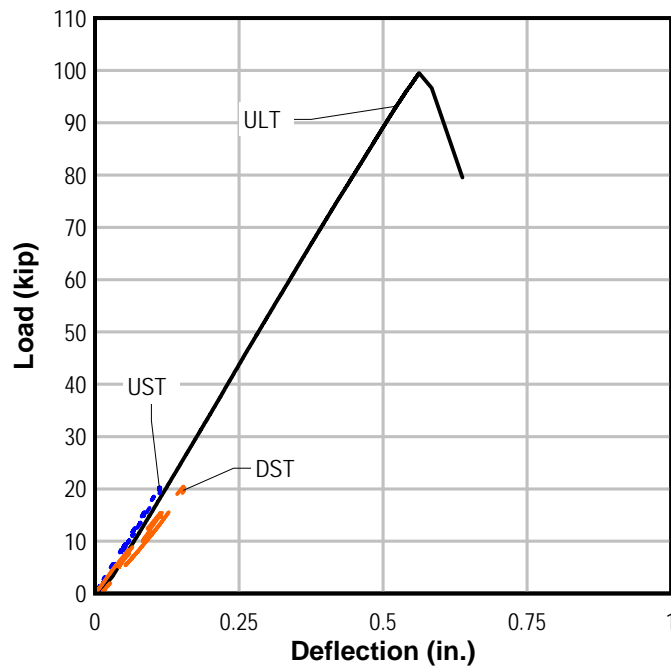


Figure 6-17. Load-displacement plot C\_P tests.

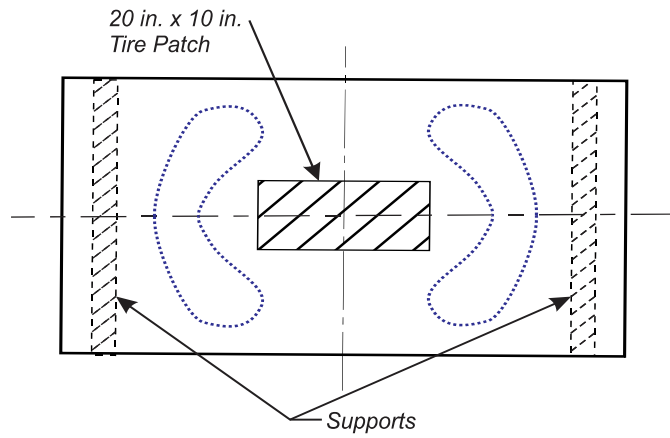


Figure 6-18. Debonded zone C\_P.

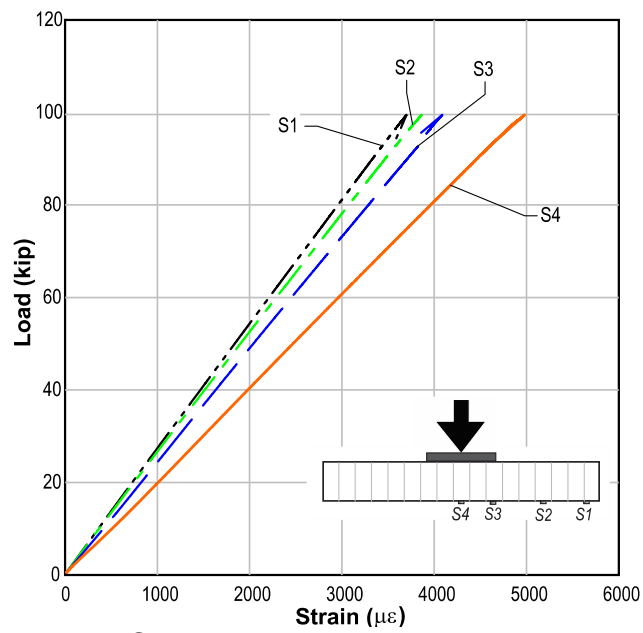


Figure 6-19. Load-strain plot C\_P ULT.

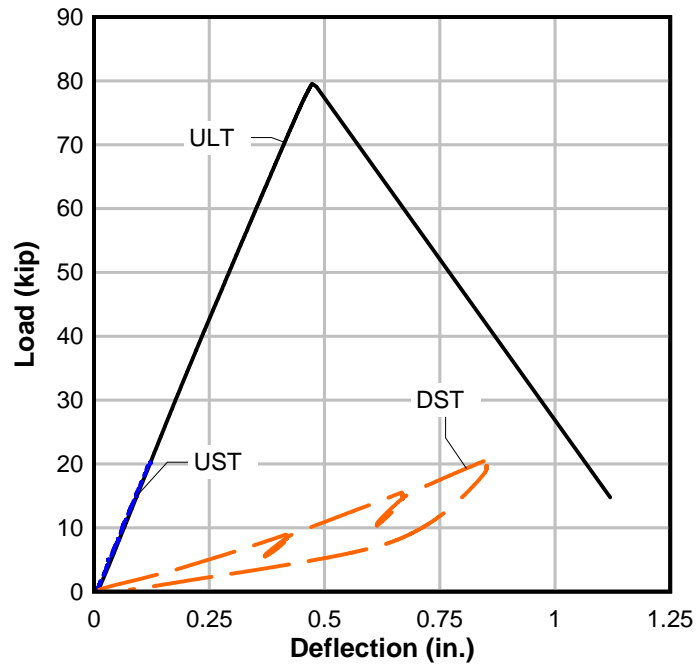


Figure 6-20. Load-displacement plot C\_N tests.



Figure 6-21. Debonding failure C\_N.

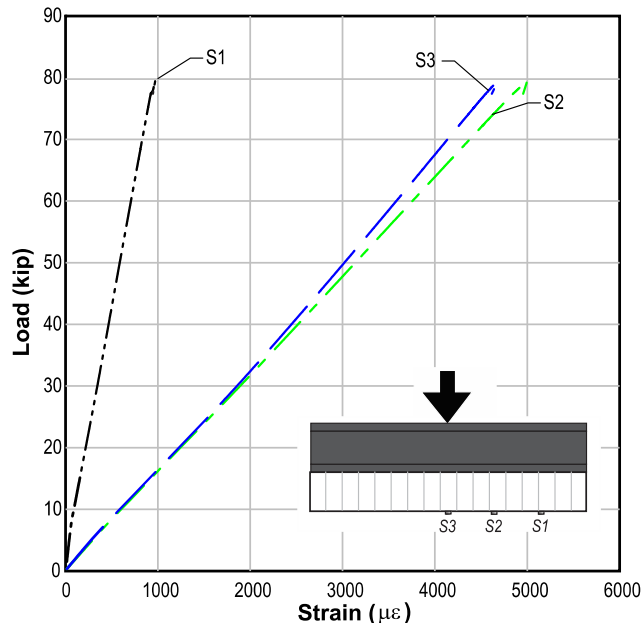


Figure 6-22. Load-strain plot C\_N ULT.

Table 6-1. A\_P stiffness.

Deck Loading	Stiffness (kip/in)	Stiffness Ratio
UST	114	1
ULT	111	0.97
DST	83	0.73

Table 6-2. A\_N stiffness.

Deck Loading	Stiffness (kip/in)	Stiffness Ratio
UST	114	1
ULT	113	0.99
DST	110	0.96

Table 6-3. B\_P stiffness.

Deck Loading	Stiffness (kip/in)	Stiffness Ratio
UST	117	1
ULT	116	0.99
DST	82	0.70

Table 6-4. B\_N stiffness.

Deck Loading	Stiffness (kip/in)	Stiffness Ratio
UST	140	1
ULT	120	0.86
DST	34	0.24

Table 6-5. C\_P stiffness.

Deck Loading	Stiffness (kip/in)	Stiffness Ratio
UST	181	1
ULT	184	1.01
DST	128	0.70

Table 6-6. C\_N stiffness.

Deck Loading	Stiffness (kip/in)	Stiffness Ratio
UST	169	1
ULT	172	1.01
DST	24	0.14

## CHAPTER 7 ANALYSIS OF AE TEST DATA USING RECOVERY RATIO ANALYSIS

This chapter covers the analysis of AE data gathered during structural testing of the deck specimens. Either the adaptation of an existing method or develop a new evaluation procedure was needed so that the AE data could be used to evaluate the structural integrity of a GFRP deck. Intensity analysis was developed for and is still in use by the railroad tank industry for inspecting steel rail cars; it uses the cumulative signal strength and changes in signal strength to determine structural integrity. This method was used initially to evaluate the AE data, but with limited success.

Recovery ratio analysis was developed for this project by adapting calm ratio, which has been used to evaluate reinforced concrete structures (Grosse and Ohtsu 2008). Luo et al. (2004) and Ohtsu et al. (2002) both used the calm ratio to evaluate cracking in concrete structures. The calm ratio is the ratio of a selected feature AE activity during the unloading to the AE activity during the loading. This approach requires that the strain be measured at or near the AE sensor to ensure that the local peak strain is identified; loading and unloading AE data are then apportioned appropriately based on the peak strain. Ohtsu et al. (2002) used load in laboratory testing of prestressed concrete beams to index the key points needed for the analysis. Other strain related parameters such as load or displacement have also been used to index the data. Luo et al. (2004) applied the calm ratio to a load test on an in-situ bridge pier using displacement as the indexing factor.

Structural evaluation using the calm ratio also requires that the load ratio be determined, which is based on the Felicity effect and is the ratio of the load at the onset of AE activity to the maximum load experienced by the specimen. Ohtsu used the load

ratio in his investigation because it is appropriate for laboratory settings where the load is known. Load history for in-service bridge components, however, is unknown. To circumvent load measurement, Luo proposed using the RTRI ratio (ratio of the Repeated Train load at the onset of AE activity to Relative maximum load for Inspection period) be used in place of the load ratio; it uses the ratio of displacement at the onset of AE activity to the peak displacement seen in the current load cycle. This differs from the load ratio in that a relative value is used instead of the maximum load ever experienced.

To evaluate the level of damage in the structure using AE, Ohtsu suggested plotting the calm ratio along the ordinate and load ratio along the abscissa. From empirical data the ratios are divided into damaged and undamaged groups. These values are plotted as vertical and horizontal lines on the plot, dividing the plot into quadrants corresponding to the severity of the damage. The top right quadrant would have the most significant damage and the bottom left quadrant would define the least amount of damage. Leaving the other two quadrants as the intermediate damage level. A high calm ratio combined with a low load ratio is indicative of heavy damage. A large amount of AE data during unloading (high calm ratio) is typically indicative of significant damage; this combined with AE activity at low loads (low load ratio) is a strong indicator of damage.

The goal of the present research was to determine if AE could be used to detect damage in GFRP deck panels in the laboratory and then eventually in the field during bridge load tests. To that end recovery ratio analysis was developed by adapting procedures by Ohtsu 2002 and Luo 2004 for use in the laboratory deck. The relative

load ratio (RL) ((7- 1) is defined as the ratio of the load at onset of AE activity to the maximum load during each loading cycle:

$$RL = \frac{ILD}{MLD} \quad (7- 1)$$

where ILD is the load at which significant AE activity is detected, and MLD is the maximum load level of the load cycle. The AE ratio (AEr) is a hit-based parameter and can be calculated as follows:

$$AEr = \frac{ULH}{LDH} \quad (7- 2)$$

where ULH is the number of hits during the unloading of the sample and LDH is the number of hits during the loading.

Eight channels of AE data were collected during testing of both undamaged (UST) and damaged (DST) specimens. Recall that service loads were used, which simulate the type of loading that would be used to generate AE in the field. Figure 7-2 (a) shows the hits recorded during DST on specimen B. To remove spurious hits, the modified Swansong 2 filter was used (Figure 7-3). This is typically used in pressure tank industry to remove known mechanical noises from the data (Association of American Rail Roads 1998). Any hit with a duration longer than 3.5 milliseconds and amplitude within 10 dB of the threshold is ignored along with all hits occurring within  $\pm \frac{1}{2}$  sec of the selected hit. This approach removes long-duration hits, which are typically indicative of rubbing and not resin cracking or fiber rupture. In this investigation only the hits known to be the rubbing are removed and the one second window around the hit was not removed. All hits with zero energy were also removed from the data set. In the example shown in

Figure 7-2 filtering removed approximately 60% of the hits. From the filtered data the AE ratio and the relative load ratio were then calculated for all the tests.

Figure 7-4 illustrates the parameters used in the RRA and the method used to calculate AEr and RL. The analysis is conducted for each channel; each analysis produces a single set of values that can be used to evaluate whether damage has occurred.

Average AEr results for DST for both positive and negative bending test for all samples are plotted in Figure 7-5 A & B. The UST AEr average values for most of the samples were considerably less than the DST values, indicating that RRA evaluation technique can consistently distinguish between damaged and undamaged specimens. Only one sample (B\_N UST) did not have the same trend as all the other samples. It is not clear why the undamaged specimen generated more AE than the damaged specimen. That particular sample only had one DST which was valid for use in the evaluation. In general, however, the method provided excellent discrimination between damaged and undamaged laboratory specimens.

Figure 7-6 shows the results from RRA for positive bending test. Respective damaged (hollow markers) and undamaged (solid markers) values are plotted. As noted previously, the results from all three decks have distinctive differences between results from damaged and undamaged decks. The various failure mechanisms and the varying severity of damage explain the large range of DST results. The UST AEr results were exclusively grouped in the lower range of the plot, this was the pattern used to develop the proposed pass-fail line, highlighted in blue in Figure 7-6. Specimens A and B appear to have some difference in the relative loading ratio, but

specimen C does not. More testing should be performed in the varying damage levels for the development of a pass fail criterion.

Figure 7-7 shows the negative bending UST and DST results. The negative bending appeared to have good discrimination for both positive and negative bending. Consequently, two sets of damage regions were proposed based on the results and are depicted by the blue lines. UST RRA results were grouped below an AEr of 0.2 with one outlier at 0.6 for sample A. This configuration did present a pattern in relation to the relative load axis. The DST results all plotted below 0.1 relative loads. A larger sample group will need to be considered in order to confirm these findings.

Table 7-1 shows the average AE evaluation results with the stiffness and strength ratios. These ratios provide a metric for comparing the damage levels sustained by each of the decks; lower ratios indicate more severe damage. The damage data do not appear to be correlated with the AE evaluation results.

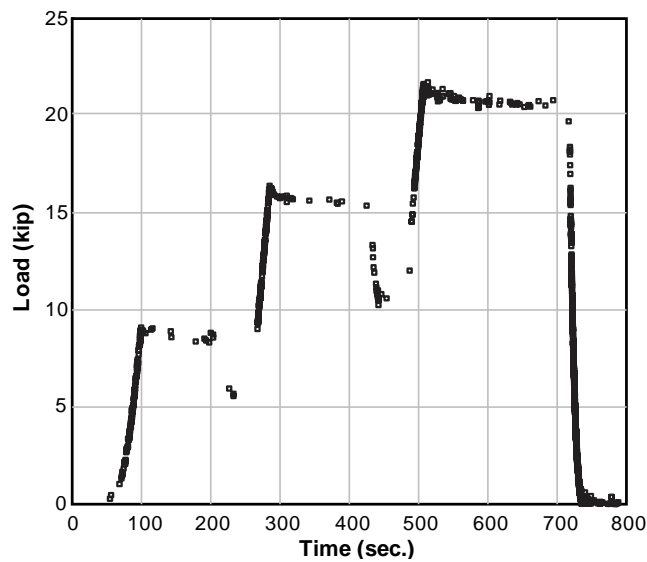


Figure 7-2. Specimen B\_P AE data unfiltered.

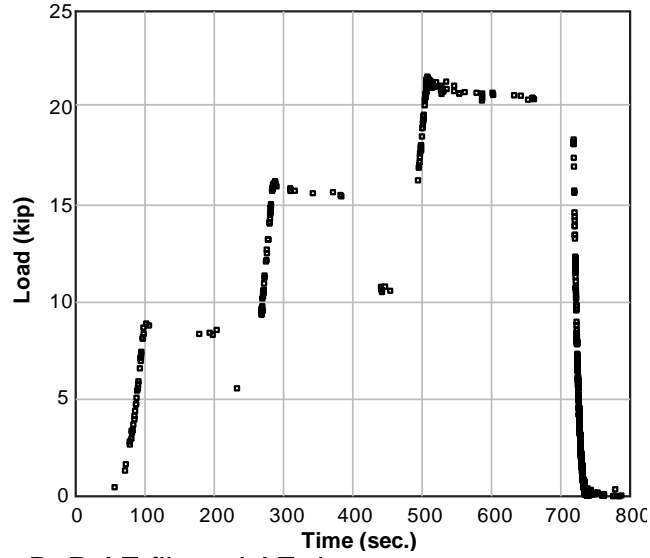


Figure 7-3. Specimen B\_P AE filtered AE data.

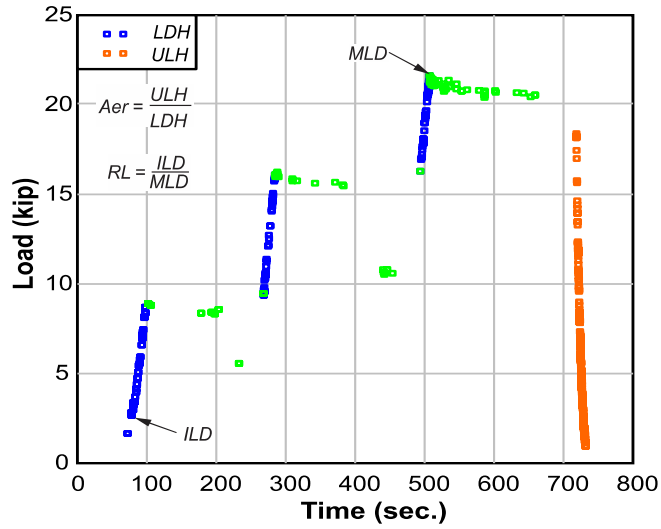


Figure 7-4. Filtered data used in AE ratio analysis calculations.

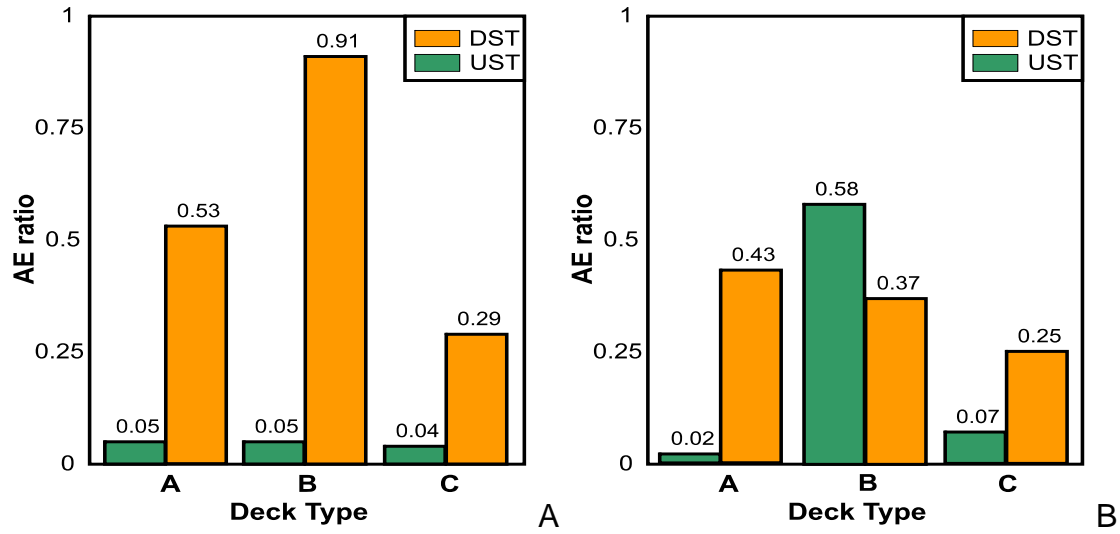


Figure 7-5. Average DST and UST values for A) positive and B) negative bending tests.

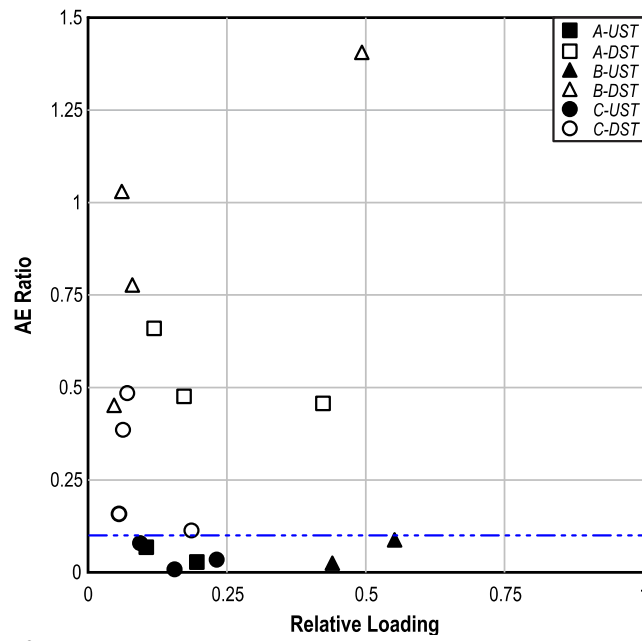


Figure 7-6. RRA plot for positive bending tests – all specimens.

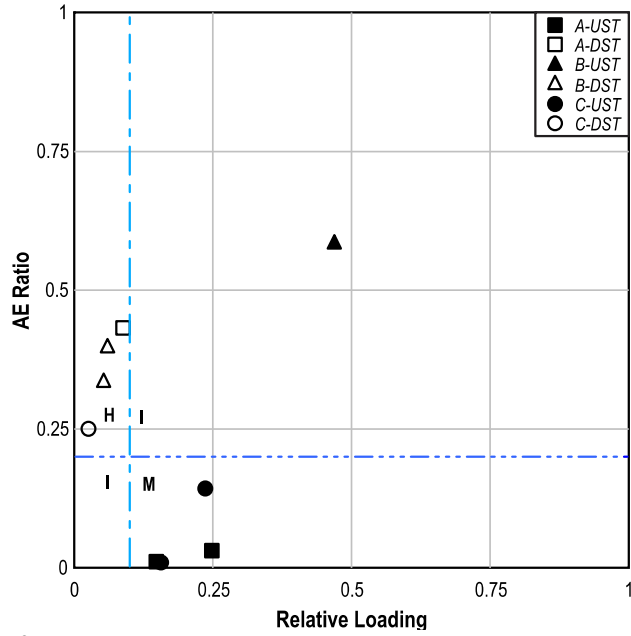


Figure 7-7. RRA plot for negative bending tests – all specimens.

Table 7-1. Average values from RRA and stiffness and strength ratio.

Specimen	AEr (avg.)		RL (avg.)		Stiffness ratio	Strength Ratio
	UST	DST	UST	DST		
A_P	0.05	0.53	0.15	0.24	0.73	0.60
A_N	0.02	0.43	0.20	0.09	0.96	0.83
B_P	0.05	0.91	0.50	0.17	0.70	0.82
B_N	0.58	0.37	0.47	0.06	0.24	0.51
C_P	0.04	0.29	0.16	0.09	0.70	0.80
C_N	0.07	0.25	0.20	0.03	0.14	0.18

## CHAPTER 8 BELLE GLADE TEST

In a related FDOT research project, a steel deck of a bridge over the Hillsboro Canal in Belle Glade Florida was replaced with Deck A (McCall et al. 2011). The deck was load tested using strain and displacement gages; during this load test AE data were also recorded. Trucks typically use lanes 1 and 2 to deliver sugarcane to the refineries north of the bridge during the harvest (Figure 8-1). These lanes were tested during the load test because of the large loads experienced compared to the South bound lanes. Strain and displacement gages were placed along the north bound lanes. AE sensors were located near strain gages. Details of the test procedures can be found in McCall et al. (2011).

### **Sensor Locations**

Figure 8-2 is a diagram of the bridge deck placement and the location of the AE sensors on the bridge relative to the deck panels. B9 and B10 are the panels monitored during the load test. The numbered lines running along the direction of travel represent the steel girders of the bridge. Table 8-1 lists the AE sensors identifications and the coordinates corresponding to the location of each sensor on the soffit of the deck.

### **Relative Ratio Analysis on Belle Glade Bridge Data.**

The Relative Ratio analysis procedure developed to analyze the AE results from the laboratory testing requires that the peak load be known so that RL can be calculated, which may not be known during a bridge test. Another parameter that may be used to mark peak load is wheel position. The influence of the load on the area of interest can be obtained from the combination of GPS and strain gage data at the AE

sensor location. This approach is particularly suited to bridge testing using GPS truck positioning in which the position of the wheel relative to the sensor is known.

The best approach would be to use the wheel position to calculate the Relative Load ratio. Unfortunately, the wheel location relative to the AE sensor position was not recorded. Figure 8-3 illustrates the adjustment made to the Relative Ratio analysis procedure to accommodate the constraints of the bridge test. RRA was adjusted so that the strain at the sensor caused by the rolling load rather than the position of the rolling load was used. The Influence ratio is defined as the ratio of the strain at the onset of AE activity to the relative maximum strain of the loading.

Each wheel load passing the AE sensors could be used in the RRA because each represents the loading and unloading of the deck. Figure 8-4 show the hits recorded during the load test for one pass of the truck over a single AE sensor. Each grouping represents the load imposed by one of the five truck axles. Although RRA could be used for any of the wheel loads, only the front and rear axles were selected for analysis. The front wheel was chosen because the data for this load was not influenced by any adjacent loads. The rear axle was also chosen because it transmits the largest wheel load.

Figure 8-5 shows a summary of the RRA results for the sampled loadings for truck position one; the AE ratio was calculated estimating the point of peak load from the AE data. Even though all the channels were used in the collection of the data, only channels 1-4 registered hits during the loading due to the attenuation of the emissions across the deck.

AE ratios results for all the load levels ranged from 0.3 to 0.8. These results demonstrate the potential of the analysis to be used in the evaluation of bridge decks. The exact wheel position with reference to the sensor was not known for the load test, due to the large number of hits near what was believed to be the peak of the load the ratios may shift. The front axle results were above the 0.5 line and all the rear axle results were less than 0.5. These results suggest that the proximity of other wheels may have an effect on the calculated AE ratio. It is also possible that grout cracking may have influenced the AE recorded during the bridge test.

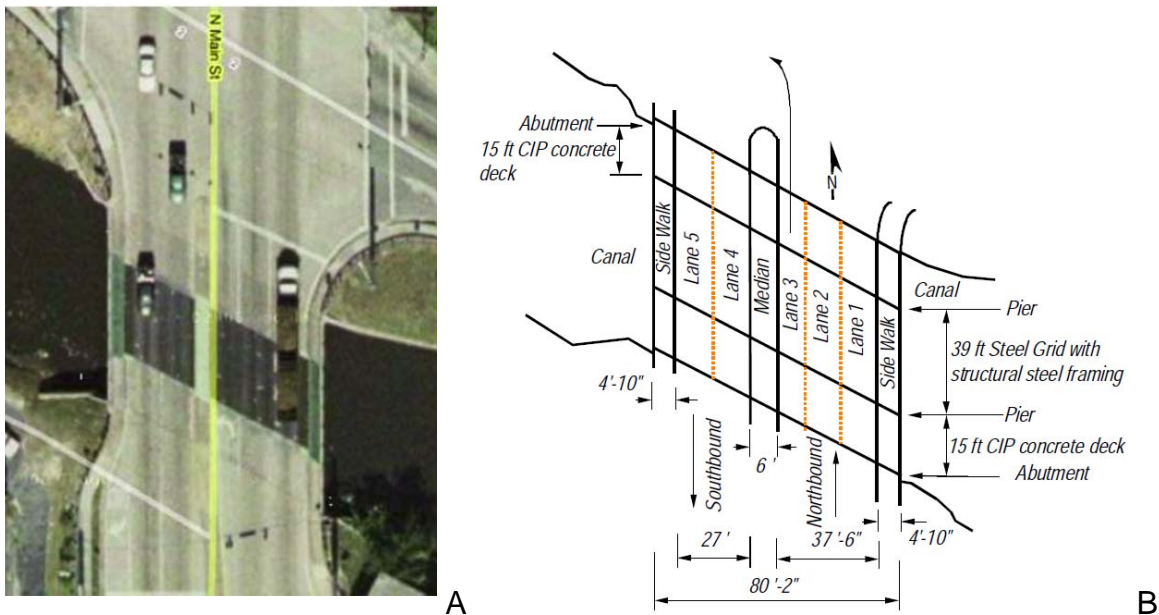


Figure 8-1. Bridge site A) aerial photo and B) detailed site plan.

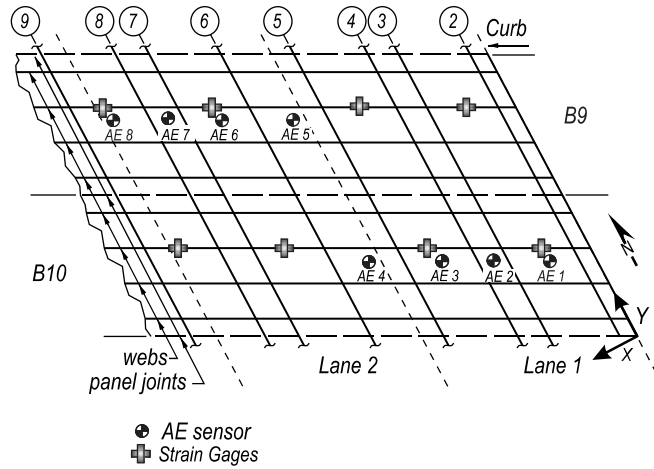


Figure 8-2. AE sensor and strain gage locations on the deck panels.

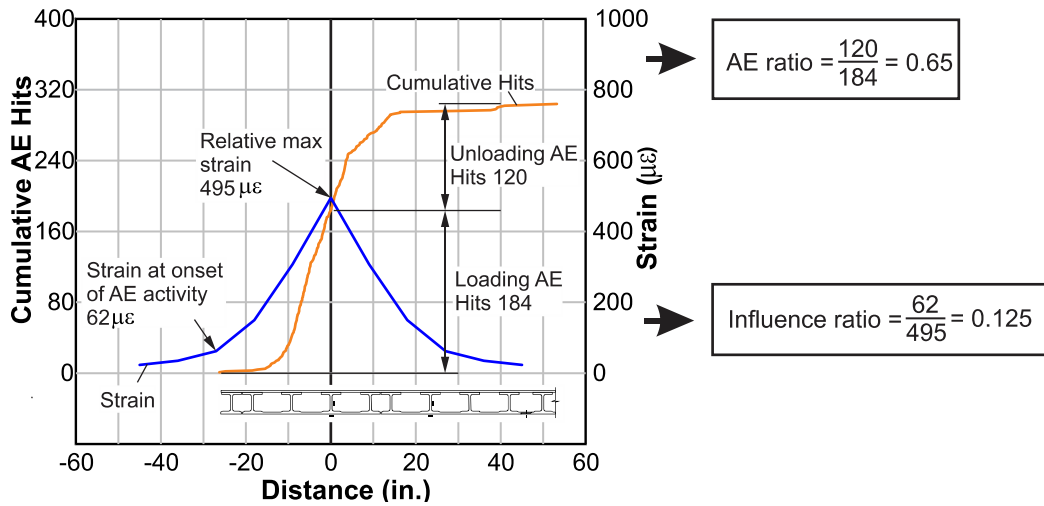


Figure 8-3. AE and influence ratio calculations for LC 4 front wheel.

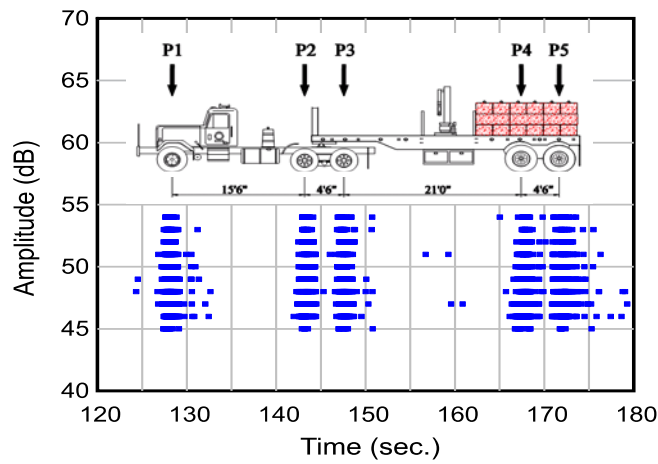


Figure 8-4. AE data from bridge test LC4.

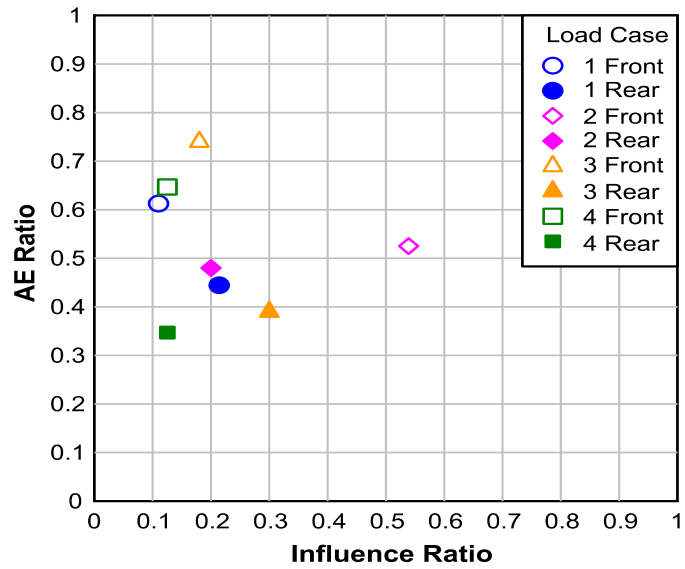


Figure 8-5. Sample RRA results for bridge load test.

Table 8-1. AE sensor identification and coordinates.

Sensor	Sensor part number	Panel ID	Coordinate (in.)	
			X-coordinate	Y-coordinate
AE 1	BD 45	B10	36	188
AE 2	BD 32	B10	70	206
AE 3	BD 36	B10	104	224
AE 4	BD 48	B10	152	250
AE 5	BD 34	B9	152	282
AE 6	BD 42	B9	200	307
AE 7	DM 09	B9	234	325
AE 8	BD 43	B9	268	344

## CHAPTER 9 SUMMARY AND CONCLUSIONS

Three commercially available GFRP bridge decks were tested in both positive and negative bending in a three-point loading setup. Each specimen was subjected to sequential load tests having the following characteristics. First, the specimen was subjected to two undamaged service tests (UST) composed of three load holds. The specimen was then subjected to an ultimate load test (ULT) in which the specimen was loaded to its ultimate capacity to cause damage without completely destroying the specimen. Finally, stepwise service loads were again imposed on the damaged deck to determine how well AE could detect the damage that had been imposed by the ultimate strength test. This test is referred to as the damaged service test (DST). Both positive and negative bending specimens were tested using the same procedures and load steps were separated by a brief load reduction to allow observation of Kaiser and felicity effects during reloading. During load testing AE, load, strain, and displacement were monitored. Strain and displacement data were evaluated.

Two AE analysis methods were used to evaluate the data. Intensity analysis, which is routinely used in the testing of pressure vessels and has been tested on GFRP decks, was used initially to analyze the AE data from the load tests. In addition, relative ratio analysis (RRA) was developed and applied to the laboratory results. RRA was also used to analyze selected bridge load test data from Belle Glade.

Three repair procedures were developed and applied to Deck A. Repair A1 was to place GFRP bars in the cavities between the webs and then fill this cavity with concrete. A2 was to apply wet layup GFRP to the damaged webs. A3 was to fill the cavities with grout and apply GFRP to the soffit of the deck.

From the previously described testing the following conclusions are drawn:

- Flexural capacity and damage characteristics of each sample were determined for both positive and negative bending in each of the three deck types. The ultimate capacity was found to be well beyond the maximum service wheel loads and ranged from 3.8 to 6.7.
- Deck A retained 60% and 83% of its positive and negative bending capacity, respectively. Deck B retained 82% and 51% of its positive and negative bending capacity, respectively. Deck C retained 80% and 14% of its positive and negative bending capacity, respectively.
- Recovery ratio analysis provided significant discrimination between AE data taken from undamaged and damaged decks. For positive bending, damaged decks generally exhibited an AE ratio of 0.1 or greater, while undamaged results were below 0.1. For negative bending, those specimens with an AE ratio greater than 0.2 and a Relative Loading less than 0.1 were damaged, while nearly all those with an AE ratio less than 0.2 were undamaged.
- Recovery ratio analysis was applied to AE data gathered from a bridge load test on a bridge with Deck A. The results, when compared to the criteria developed for the laboratory tests indicated damage. No deck damage was noted. Refinement in the method may be needed or cracking of the grout pad used to support the GFRP deck system may be leading to false positive readings.

## LIST OF REFERENCE

- Alagusundaramoorthy, P., Harik, I. E., and Choo, C. C. (2006). "Structural Behavior of FRP Composite Bridge Deck Panels", *J. Bridge Eng.*, 11(4), 384-393.
- Arnold, R. E. (2003). Acoustic Emission Evaluation of FRP Composite Specimens in Tension and Bending. Morgantown, W. Va.: West Virginia University *College of Engineering and Mineral Resources*. West Virginia University.
- Asencio, R. and Hamilton, H. R., (2011) "Damage Detection and Repair Methods for FRP Bridge Decks." Vol. 1, FDOT Research Report BDK-75-977-17.
- Association of American Railroads (1998). "Procedure for Acoustic emission evaluation of tank cars and IM101 tanks Issue 6." Operations and maintenance department-mechanical division.
- Brown, D. L., and Berman, J. W. (2010). "Fatigue and Strength Evaluation of Two Glass Fiber-Reinforced Polymer Bridge Decks." *J. Bridge Eng.*, 15(3), 290-301.
- Camatta, G., and Shing, P. B. (2010). "Static and fatigue load performance of a gfrp honeycomb bridge deck." *Composites:Part B* 41, 299-307
- Chen, A., and Davalos, J. F. (2010). "Strength evaluations of sinusoidal core for FRP sandwich bridge deck panels." *Composite Structures*, 92, 1561-1573
- Cole, T. A., Lopez, M., and Ziehl, P. H. (2006). "Fatigue behavior and nondestructive evaluation of full-scale FRP honeycomb bridge specimen." *J. Bridge Eng.*, 11(4), 420-429.
- Cousins, T. E., Lesko, J. J., Mjumdar, P. K., and Liu, Z. (2009). "Rapid replacement of Tangier Island bridges including lightweight and durable fiber-reinforced polymer deck systems." *FHWA/ VTRC 10-CR3*
- Fowler, T.J., Blessing, J.A. and Conlisk, P.J. (1989). "New directions in testing." *In: Proc. 3rd International Symposium on Acoustic Emission from Composite Materials*, Paris, France
- Gostautas, R., Ramirez, G., Peterman, R. J. and Meggers, D. (2005). "Acoustic Emission Monitoring and Analysis of Glass Fiber-Reinforced Composites Bridge Decks." *J. Bridge Eng.*, 10 (6), 713-721.
- Grosse, C. U., & Ohtsu, M. (2008). Acoustic Emissions Testing. *Springer-Verlag Berlin Heidelberg*.
- Hong, T., & Hastak, M. (2006) Construction, Inspection, and Maintenance of FRP Deck Panels. *Journal of Composites for Construction*, 10 (6), 561-572.

- Kalny, O., Peterman, R. J., and Ramirez, G., (2004). "Performance evaluation for repair technique for damaged fiber-reinforced polymer honeycomb bridge deck panels." *J. Bridge Eng.*, 9(1), 75-86.
- Keller, T., and Gurtler, H. (2005). "Quasi-static and fatigue performance of a cellular FRP bridge deck adhesively bonded to steel girders." *Compos. Struct.*, 70, 484–496.
- Liu, Z., Cousins, T. E; Lesko, J.J., & Sotelino, E. D. (2008). Design Recommendations for a FRP Bridge Deck Supported on Steel Superstructure. *Journal of Composites for Construction*, 12(4), 660-668.
- Luo, X., Haya, H., Inaba, T., Shiotani, T., and Nakanishi, Y. (2004). "Damage evaluation of railway structures by using train-induced AE." *Construction and Building Materials* 18, 215–223.
- Majumdar, P. K., Lesko, J. J., Cousins, T. E., and Liu, Z. (2009). "Conformable tire patch loading for FRP composite bridge deck." *J. Compos. Constr.*, 13(6), 575-581.
- McCall, J. L., Peng, X., Singh, A. P., and Hamilton, H. R., (2011) "Hillsboro Canal Bridge Monitoring.", FDOT Research Report BDK-75-977-16.
- O'Connor, J. S. (June 2008), "GRP bridge decks and superstructures in the USA." *Reinforced Plastics*, 26-31.
- Ohtsu, M, Uchida, M; and Okamoto, T (2002). "Damage assessment of reinforced concrete beams qualified by acoustic emission." *ACI Structural Journal*, 99, 411-417.
- Park, K. T., Hwang, K. T., Lee, Y. H., and Kim, S. M (2007). "Performance verification of a new pultruded GFRP bridge deck-to-girder connection system." *Compos. Struct* 81 (2007) 114–124.
- Physical Acoustics Corporation (2004), "AEwin™ software users manual." Rev. 1.90, Physical Acoustic Corporation, Princeton Junction., New Jersey, USA.
- Physical Acoustics Corporation (2008), "R15I-AST sensor internal preamplifier acoustic emissions sensor." Rev. 10/05 #81-05, MISTRAS Group Inc., Princeton Junction, New Jersey.
- Prachasaree, W., Gangarao, H. V. S., and Shekar, V. (2009). "Performance Evaluation of FRP Bridge Deck Under Shear Loads". *J. Compos. Materials*, 43(4), 377-395.
- Reeve, S., (2010), "FRP bridges-14 years and counting." *Reinforced Plastics*, 40-44.

- Telang, N. M., Dumlao, C., Mehrabi, A. B., Ciolko, A. T., and Gutierrez, J. (2006). "Field inspection on in-service FRP bridge decks." (No. 564). *Transportation Research Board*.
- Turner, M. K., Harries K. A., Petrou, M. F., Rizos, D.(2004). "In situ structural evaluation of a GFRP bridge deck system." *Compos. Struct.*, 65, 157–165.
- Vyas, J. S., Zhao, L., Ansley, M. H., and Xia, J. (2009). "Characterization of a low-profile fiber-reinforced polymer deck system for moveable bridges." *J. Bridge Eng.*, 14(1), 55-65.

## BIOGRAPHICAL SKETCH

Rafael Asencio received an Associate of Science from Santa Fe Community College in Automotive Technologies, in 2001. Rafael received a Bachelor of Science in Civil Engineering in 2009 and a Master of Engineering in Civil Engineering in 2011 from the Civil and Coastal Engineering Department at the University of Florida.